Accretion Disk Size Measurement and Time Delays in the Lensed Quasar WFI 2033–4723

Christopher W. Morgan[1], Gregory E. Hyer[1], Vivien Bonvin[2], Ana M. Mosquera[1], Matthew Cornachione[1], Frederic Courbin[2], Christopher S. Kochanek[3,4] and Emilio E. Falco[5]

ABSTRACT

We present 13 seasons of R-band photometry of the quadruply-lensed quasar WFI 2033-4723 from the 1.3m SMARTS telescope at CTIO and the 1.2m Euler Swiss Telescope at La Silla, in which we detect microlensing variability of $\sim$ 0.2 mags on a timescale of $\sim$6 years. Using a Bayesian Monte Carlo technique, we analyze the microlensing signal to obtain a measurement of the size of this system's accretion disk of $\log(r_s/\mathrm{cm}) = 15.86^{+0.25}_{-0.27}$ at $\lambda_{rest} = 2481$Å, assuming a 60° inclination angle. We confirm previous measurements of the BC and AB time delays, and we obtain a tentative measurement of the delay between the closely spaced A1 and A2 images of $\Delta t_{A1A2} = t_{A1} - t_{A2} = -3.9^{+3.4}_{-2.2}$ days. We conclude with an update to the Quasar Accretion Disk Size – Black Hole Mass Relation, in which we confirm that the accretion disk size predictions from simple thin disk theory are too small.

Subject headings: gravitational lensing: strong — gravitational lensing: micro — accretion disks — quasars: individual (WFI 2033-4723)

1. INTRODUCTION

Gravitationally lensed quasars provide a wealth of resources to observers. Their utility in cosmology was realized quite early on (e.g. Refsdal 1964), and a number of collaborations

[1]Department of Physics, United States Naval Academy, 572C Holloway Rd, Annapolis, MD 21402, USA; cmorgan@usna.edu

[2]Laboratoire d'Astrophysique, École Polytechnique Fédérale de Lausanne (EPFL), Observatoire, 1290 Sauverny, Switzerland

[3]Department of Astronomy, The Ohio State University, Columbus, OH 43210, USA

[4]Center for Cosmology and Astroparticle Physics, The Ohio State University, Columbus, OH 43210, USA

[5]Harvard-Smithsonian Center for Astrophysics, 60 Garden St, Cambridge, MA 02138, USA

(e.g. *COSMOGRAIL*, Courbin et al. (2005) & *H0LiCOW*[1]) continue to pursue measurements of lensed quasar time delays to make independent measurements of the Hubble Constant, H_0 (e.g. Kochanek 2002; Vuissoz et al. 2008; Fohlmeister et al. 2013; Suyu et al. 2017; Bonvin et al. 2017) and a range of other useful cosmographic measurements. Quasar microlensing, also predicted quite some time ago (e.g. Chang & Refsdal 1979), provides additional motivation for monitoring lensed quasars since the analysis of microlensing variability (e.g. Kochanek 2004; Morgan et al. 2006; Poindexter et al. 2007; Morgan et al. 2010; Hainline et al. 2013; MacLeod et al. 2015) and chromatic flux ratio anomalies (e.g. Pooley et al. 2007; Bate et al. 2008, 2011; Mediavilla et al. 2011; Pooley et al. 2012; Schechter et al. 2014) can be analyzed to probe the central engines of the quasars and the properties of the lens galaxy.

The quadruply lensed quasar WFI J2033-4723 (hereafter WFI2033; $20^h33^m42.08^s$, -47°23'43.0" [J2000.0]) was discovered during a wide-field imaging survey for lensed quasars in the southern hemisphere using the MPG/ESO 2.2 m telescope (Morgan et al. 2004). It has a source redshift of $z_s = 1.66$, a lens redshift of $z_l = 0.661$ (Eigenbrod et al. 2006) and a maximum image separation of $2\farcs5$. Vuissoz et al. (2008, hereafter V08) used three seasons (2004-2007) of monitoring data from the Small and Moderate Aperture Research Telescope System (SMARTS) 1.3m telescope at the Cerro Tololo Inter-American Observatory (CTIO) and the 1.2m Leonhard EULER Swiss telescope at La Silla, Chile to measure time delays of $|\Delta t_{B-A}| = 35.5 \pm 1.4$ days and $|\Delta t_{B-C}| = 62.6^{+4.1}_{-2.3}$ days between the merged A1+A2 = A, B and C images. V08 found no evidence of variability due to extrinsic factors such as microlensing. Recently, however, Giannini et al. (2017) made a robust detection of microlensing in their 4-season monitoring campaign using the 1.54m Danish telescope at La Silla, a result which we independently corroborated in this investigation. Most recently, Motta et al. (2017) used the single-epoch chromatic microlensing technique to make estimates of the size of the central engine and broad line region in WFI2033.

In this paper, we combine 9 new seasons of WFI2033 monitoring data with the 4 seasons of data from V08 to create a 13-season set of light curves. We present our observational data and reduced light curves in §2, and we analyze the full combined light curves in §3 to confirm the V08 time delays and measure the A1–A2 delay for the first time. In §4 we describe our microlensing analysis technique to include the properties of our strong lens models for WFI2033. In §5, we present the results of our analysis, and we discuss their implications for accretion disk theory. Throughout our discussion we assume a flat cosmology with $\Omega_{\rm M} = 0.3$, $\Omega_\Lambda = 0.7$, and $H_0 = 70\,{\rm km\,s^{-1}}$ Mpc^{-1} (Hinshaw et al. 2009).

[1]http://www.h0licow.org

2. OBSERVATIONAL DATA

2.1. *HST* Imagery

We observed WFI2033 in the V- (F555W), I- (F814W) and H- (F160W) bands using the *Hubble Space Telescope* (*HST*) as an element of the the CfA-Arizona Space Telescope Survey (CASTLES[2], Lehár et al. 2000). The V- and I-band images were taken using the Wide-Field Planetary Camera 2 (WFPC2). The $H-$band images, originally presented in V08, were taken using the Near-Infrared Camera and Multi-Object Spectrograph (NICMOS). We fit the astrometry and photometry of the lens in the *HST* imagery with the *imfitfits* (Lehár et al. 2000) routine, using a de Vaucouleurs model for the lens galaxy G1, an exponential disk model for the quasar host galaxy and point sources for the quasar images. Our astrometric and photometric fits, consistent with those made independently by V08, are presented in Table 1.

2.2. Monitoring Observations

On the 1.3 m SMARTS telescope we used the optical channel of the dual-beam ANDICAM instrument (DePoy et al. 2003),which has a plate scale of $0\farcs369$ pixel^{-1} and a $6\farcm5 \times 6\farcm3$ field of view. The mean sampling of the SMARTS data is one epoch every eight days, with three 300 s exposures at each epoch using the R-band filter. The R-band filter has an effective wavelength of 658 nm, translating to a rest-frame wavelength of 2473 Å in the UV. The

[2]http://cfa.harvard.edu/castles/

Table 1. HST Astrometry and Photometry of WFI 2033–4723

Component	Astrometry		Photometry		
	ΔRA	ΔDec	H=F160W	I=F814W	V=F555W
A1	$-2\farcs196 \pm 0\farcs003$	$1\farcs261 \pm 0\farcs003$	17.22 ± 0.02	18.15 ± 0.05	19.24 ± 0.03
A2	$-1\farcs482 \pm 0\farcs003$	$1\farcs376 \pm 0\farcs003$	17.60 ± 0.02	18.65 ± 0.13	19.26 ± 0.09
B	$\equiv 0$	$\equiv 0$	17.85 ± 0.02	18.63 ± 0.14	19.24 ± 0.04
C	$-2\farcs114 \pm 0\farcs003$	$-0\farcs277 \pm 0\farcs003$	17.90 ± 0.02	18.82 ± 0.03	19.53 ± 0.02
G1	$-1\farcs438 \pm 0\farcs006$	$0\farcs308 \pm 0\farcs009$	17.46 ± 0.00	19.69 ± 0.03	22.51 ± 0.28

SMARTS dataset consists of 117 epochs between March 2004 and August 2017.

On the 1.2 m EULER telescope we used the EulerCAM camera which has a plate scale of $0\farcs2149$ pixel^{-1} and a $15\farcm0 \times 15\farcm0$ field of view. The mean sampling of the EULER data is one epoch every five days, with five 360s exposures at each epoch using the 'RG' or 'Rouge Genève' filter. The RG filter is a modified broad Gunn R filter, with an effective wavelength of 660 nm translating to a rest-frame wavelength of 2481 Å. The new EULER dataset consists of 178 epochs between October 2010 and December 2016.

The details of our photometric measurement technique are discussed in Kochanek et al. (2006), but we provide a brief summary of that process here. We use five reference stars, located at $(-2\farcs4, 61\farcs4)$, $(-16\farcs1, 15\farcs3)$, $(56\farcs0, 70\farcs3)$, $(60\farcs2, -0\farcs9)$ and $(-34\farcs4, 82\farcs5)$, with respect to image A1. These reference stars are used as the basis for a three-component elliptical Gaussian point-spread function (PSF) model, which we apply to the blended quasar images to obtain the relative brightness of each component at each epoch. When applying the PSF model, we hold the relative positions of the lens components fixed to the astrometry from our *HST* H-band images. We model the lens galaxy using a nested Gaussian with fixed effective radius and flux to approximate a de Vaucouleurs profile. For the effective radius, we used our measurement from the *HST* fits $r_{eff} = 0\farcs83 \pm 0\farcs1$, and for the flux we use the value which minimizes the total χ^2 in the residuals following galaxy model subtraction when summed over all epochs. We measured a very small color offset of 0.002 magnitudes between the EULER and SMARTS photometry which we applied to the SMARTS data when creating our combined light curves and the data provided in Tables 3 and 4. Both the EULER and SMARTS images are characterized by a median stellar FWHM (seeing) of $1\farcs2$. Since the merging A1/A2 pair are separated by only $0\farcs72$, deconvolving the flux from these two images was challenging. For seeing conditions worse than $1\farcs5$ and $1\farcs62$ for SMARTS and EULER, respectively, we were unable to reliably resolve any of the quasar's images, so we were forced to discard images taken under these conditions. We also discarded 31 of the 326 total observing epochs from SMARTS and EULER due to bright sky or cloudy observing conditions. In Figure 2 we display our new light curves alongside the published light curves from V08. Since V08 were unable to reliably separate the flux from images A1 and A2, they summed the flux from this closely spaced merging pair to create a single image A light curve in which $f_A = f_{A1} + f_{A2}$.

3. TIME DELAYS

Using the polynomial light curve fitting technique of Kochanek et al. (2006), we measured the time delays between the combined image A = A1 + A2, image B and image C.

In the Kochanek et al. (2006) method, the intrinsic and extrinsic variability in the light curves are fitted by Legendre polynomials, and the polynomial order is chosen using the F-test. In the case of the delay between images A and B and images C and B, we found that a $N_{source} = 10^{\rm th}$ order polynomial provided a sufficient fit for the source variability and that a $N_{\mu} = 2^{\rm nd}$ order polynomial was appropriate for approximating and removing the microlensing variability. In Figure 3, we show the χ^2 statistic for the time delay fits. The delay measurements and their 1σ uncertainties are $\Delta t_{BA} = t_B - t_A = -35.3^{+1.3}_{-1.1}$ days and $\Delta t_{BC} = t_B - t_C = -61.3^{+2.6}_{-2.3}$ days (in the sense that image B leads both images A and C). In Figure 4, we show the light curves shifted by these delay values. These new measurements are fully consistent with those of V08.

Using our newly reduced light curves, we also obtain a tentative measurement of the delay between images A1 and A2. With a $N_{source} = 5^{\rm th}$ and $N_{\mu} = 2^{\rm nd}$ order polynomials for the intrinsic and microlensing variability, respectively, we find that image A1 leads image A2 by $\Delta t_{A1A2} = t_{A1} - t_{A2} = -3.9^{+3.4}_{-2.2}$ days. We display these results in Figure 5. While V08 were not able to measure the A1-A2 delay, they did constrain the expected range of that delay to $-1 > \Delta t_{A1A2:model} > -3$ days using a series of lens galaxy mass models. While significantly coarser than our measurement of the B-A and B-C delays, the A1-A2 measurement is consistent with the V08 lens models, although this pair will have the largest fractional uncertainties from microlensing-induced variability (Tie & Kochanek 2018). In the present paper, we generate a series of lens galaxy models in which the expected A1-A2 delay is $-1.6 > \Delta t_{A1A2(model)} > -3.3$ days, also consistent with our A1–A2 measurement. With these updated time delay measurements, we proceed to the primary goal of this investigation, the analysis of extrinsic variability from microlensing in the reduced light curves. A full analysis of the updated delays will be published in Bonvin et al. (2018).

4. MICROLENSING ANALYSIS

4.1. Lens Galaxy Models and Magnification Patterns

In essence, our Bayesian Monte Carlo technique for microlensing analysis is an attempt to reproduce the observed microlensing variability using a large set of models for the physical conditions that might have led to this variability (Kochanek 2004). All of this hinges on our ability to accurately model the conditions in the lens galaxy through which the quasar's light must pass. We started by applying the LENSMODEL code of Keeton (2001) to the astrometry from our *HST* observations to yield a range of models for the stellar and dark matter content in the lens galaxy at the positions of the lensed images. Following V08, we adopted a 2-component model for the lens galaxy (G1 in Fig. 1). Since this system

is now known to exhibit microlensing of both the continuum and the Broad Line Region (BLR) (Sluse et al. 2012; Motta et al. 2017), we did not use the *HST* flux ratios or those from our ground-based observations as a constraint on the lens galaxy mass models. We required our models to reproduce the astrometry of the lensed images, and we allowed the position, effective radius, ellipticity and position angle of the lens galaxy to vary within the uncertainties of the photometric model presented in §2.1. Consistent with V08, we were unable to model the astrometry of the lensed images unless we included the influence of the neighboring galaxy G2, the east-west shear from which cannot be created by G1 since it has an ellipticity position angle of only 25° east of north. We modeled G2 as a singular isothermal sphere whose properties were also allowed to vary within the uncertainties of our *HST* photometric and astrometric fits.

Since the dark matter content in the lens galaxy is unknown, we created a series of 10 models for the lens galaxy in which the dark matter fraction varies across an order of magnitude. We began by modeling the lens galaxy using only a de Vaucouleurs profile. In each subsequent model, we decreased the monopole moment of the stellar de Vaucouleurs component by 10% of the constant M/L model mass, and we added an extended, concentric Navarro, Frenk, & White (1996, NFW) component to model the dark matter. We parameterized this series using the quantity $f_{M/L}$, representing the fraction of the lens galaxy mass relative to the constant mass-to-light (M/L) ratio model. From this model sequence, we extract the total convergence κ, the convergence from the stars κ_*, the shear γ and the shear position angle θ_γ at the location of each lensed image. While models in the range $0.4 \leq f_{M/L} \leq 0.5$ are more consistent with our measured time delays, for completeness we use the entire model sequence in our Monte Carlo microlensing simulations because Schechter & Wambsganss (2002) demonstrated that local microlensing statistics are very sensitive to κ_*/κ. The parameters of all 10 models are presented in Table 2.

Using the inverse ray-shooting technique (as described in Kochanek et al. 2006), we generated forty random realizations of the expected microlensing magnification conditions in the vicinity of each image for each of our 10 macro models parameterized by $f_{M/L}$. The magnification patterns are 8192×8192 pixels representing a projected source plane scale of twenty $1 M_\odot$ Einstein radii or 8.66×10^{17} cm. This implies a pixel scale of 1.06×10^{14} cm in the source plane. We assumed an initial stellar mass function (IMF) of $dN(M)/dM \propto M^{-1.3}$ with a dynamic range of 50, which approximates the microlensing-based Galactic bulge IMF of Gould (2000), although Wyithe et al. (2000) and Congdon et al. (2007) show that microlensing statistics are not especially sensitive to choice of IMF.

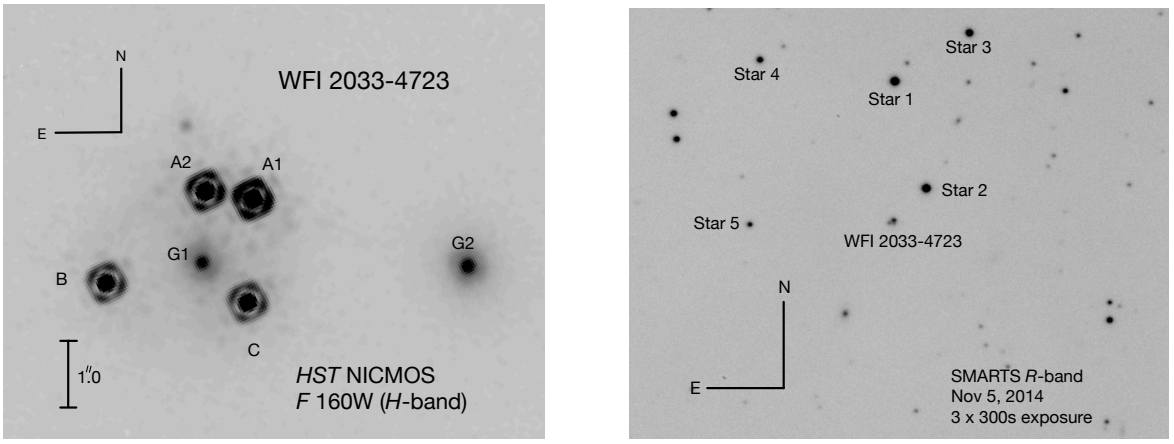

Fig. 1.— Left: *HST* H-band NICMOS image of the lensed quasar WFI 2033–4723. Images A1 and A2 are merging at a fold caustic; we expect them to have very similar time delays. Right: A stack of three 300 s R-band images from the 1.3m SMARTS telescope. The image scale is $4'33" \times 3'39"$.

Table 2. WFI2033–4723 Lens Galaxy Mass Models

$f_{M/L}$	Convergence κ				Shear γ				κ_*/κ				χ^2/N_{dof}
	A1	A2	B	C	A1	A2	B	C	A1	A2	B	C	
0.1	0.75	0.83	0.61	0.92	0.13	0.30	0.15	0.27	0.014	0.025	0.010	0.031	0.247
0.2	0.71	0.80	0.57	0.89	0.15	0.35	0.15	0.33	0.029	0.051	0.021	0.063	0.431
0.3	0.68	0.76	0.53	0.85	0.17	0.40	0.15	0.39	0.046	0.079	0.033	0.097	0.606
0.4	0.65	0.72	0.50	0.82	0.18	0.45	0.16	0.45	0.07	0.11	0.05	0.14	0.761
0.5	0.61	0.68	0.45	0.78	0.20	0.51	0.16	0.51	0.09	0.16	0.07	0.19	0.904
0.6	0.58	0.64	0.42	0.75	0.22	0.56	0.17	0.57	0.11	0.19	0.08	0.22	1.02
0.7	0.54	0.60	0.37	0.70	0.24	0.63	0.17	0.64	0.16	0.27	0.13	0.30	1.15
0.8	0.50	0.56	0.33	0.67	0.26	0.68	0.18	0.69	0.19	0.32	0.16	0.35	1.24
0.9	0.45	0.51	0.27	0.63	0.28	0.76	0.19	0.77	0.29	0.47	0.27	0.49	1.39
1.0	0.43	0.48	0.26	0.60	0.29	0.78	0.19	0.81	0.27	0.46	0.25	0.48	1.41

Note. — Convergence κ, shear γ and the fraction of the total surface density composed of stars κ_*/κ at each image location for the series of mass models. The parameter $f_{M/L} = 1.0$ is the mass of the de Vaucouleurs model for the visible lens galaxy relative to its mass in the absence of dark matter. The χ^2 per degree of freedom for each model is provided in the χ^2/N_{dof} column.

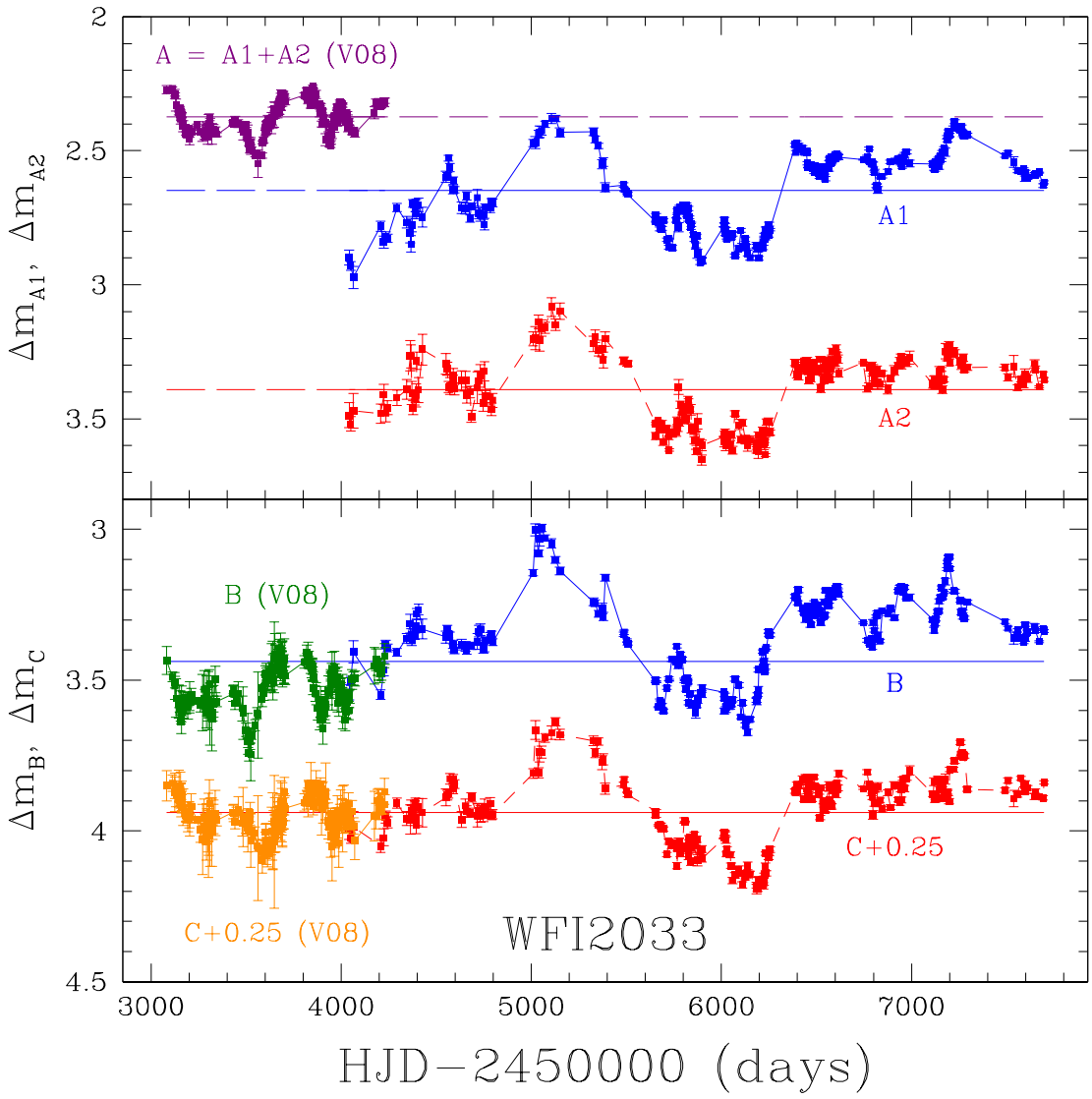

Fig. 2.— Combined light curves from WFI2033. Images A1 and A2 are shown in the top panel and images B and C are plotted in the bottom panel. The previously published light curves from Vuissoz et al. (2008) are labeled with 'V08', and in those light curves the flux from images A1 and A2 were summed. Magnitudes are relative to an arbitrary zero point.

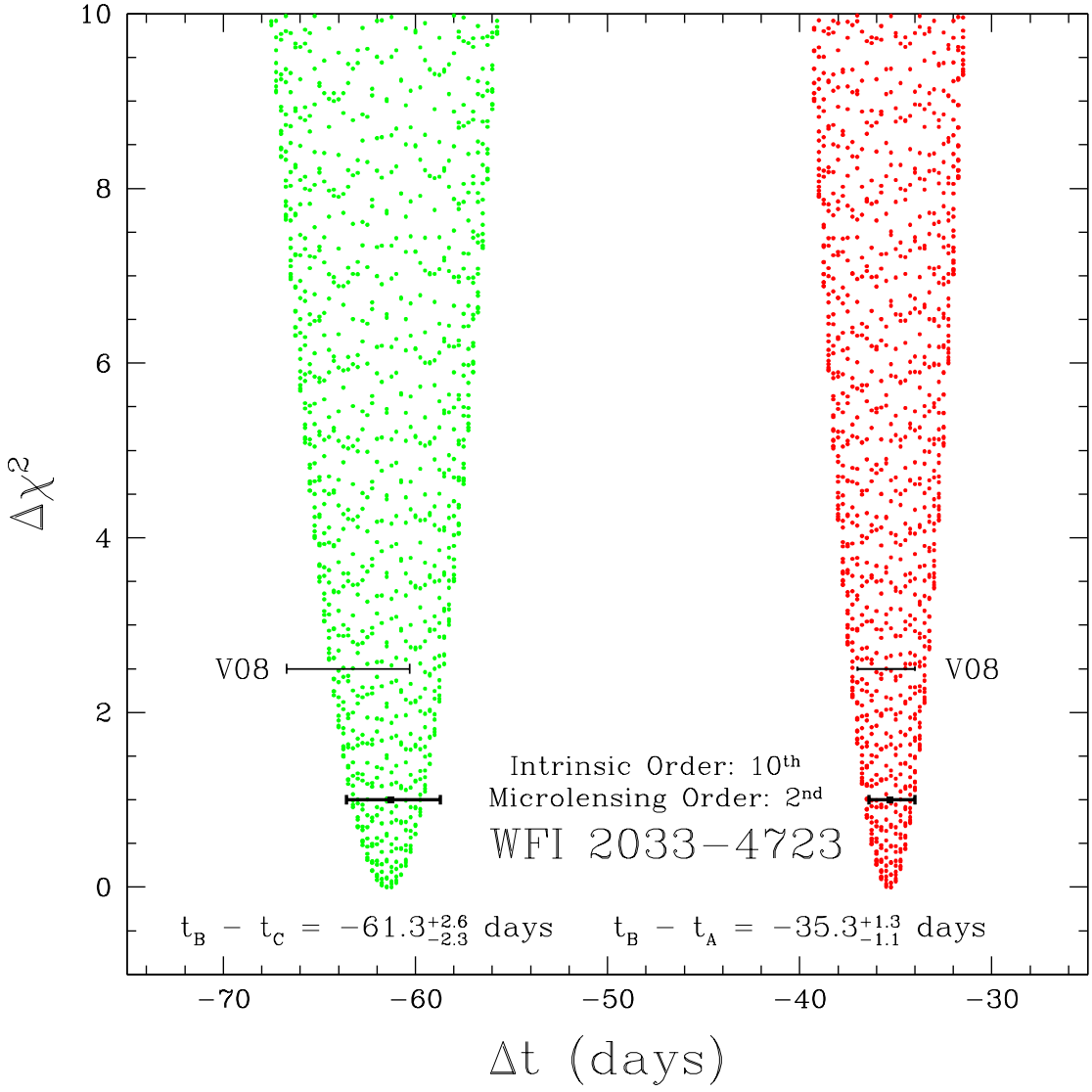

Fig. 3.— Left: χ^2 surfaces for our measurement of the time delay between images B and A = A1 + A2 and between images B and C. Delays from V08 are labeled as such, and the present results with 1σ uncertainties are plotted as heavy solid points with error bars.

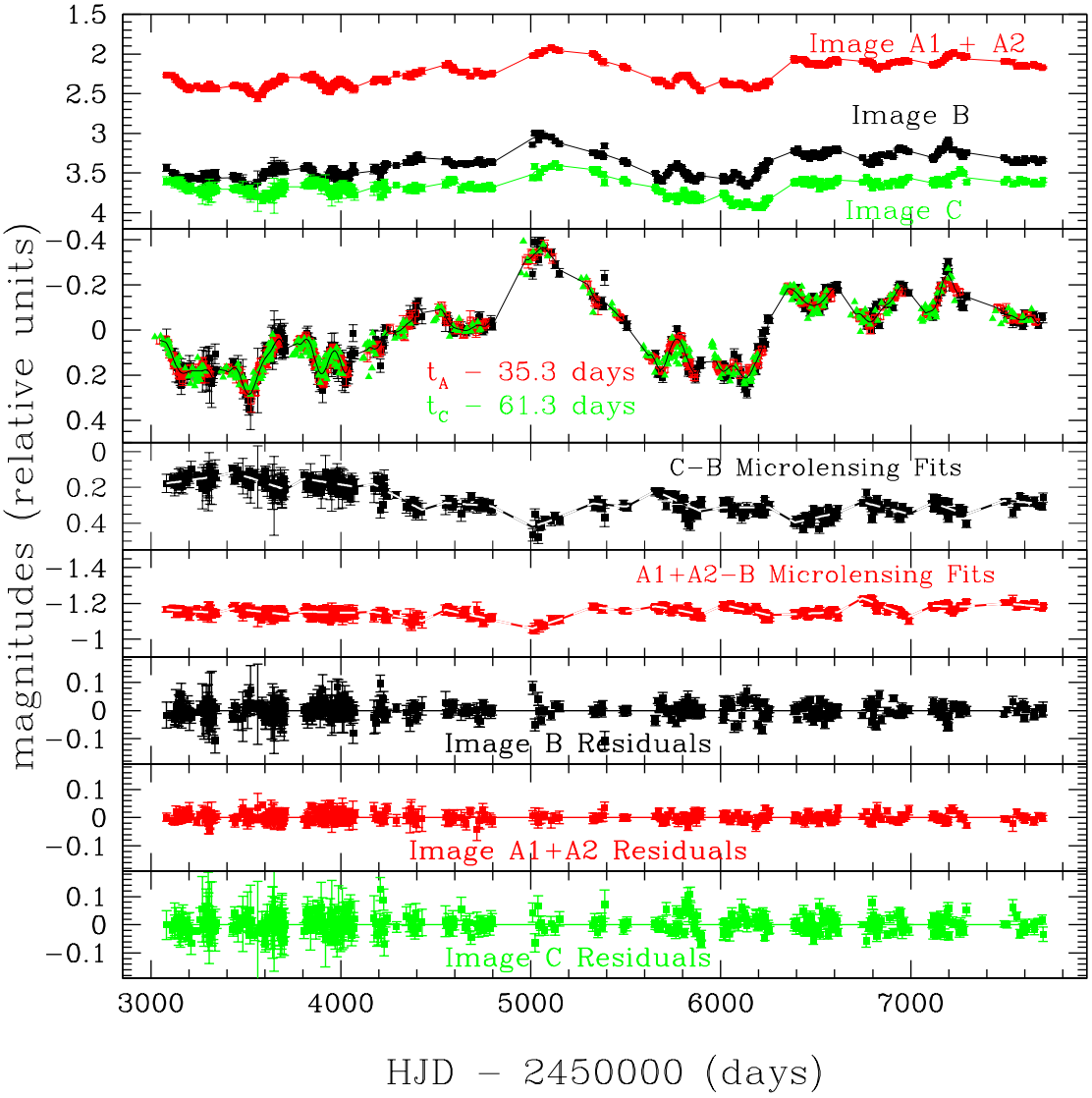

Fig. 4.— Top panel shows the raw light curves for A=A1+A2, B & C. Second panel shows time-delay shifted light curves in which the 2nd order phased polynomial fit to the microlensing variability has been removed. Third and fourth panels show the 2nd order fit to the microlensing in the difference light curves C-B and A-B. Note that the microlensing residuals in the B-C fits are significantly larger than those in the A-C fits. The light curves were also normalized to the same magnitude scale for display purposes. The solid line shows the 10th order polynomial fit of the intrinsic variability. The bottom panels show the residuals following subtraction of both the intrinsic and microlensing fits.

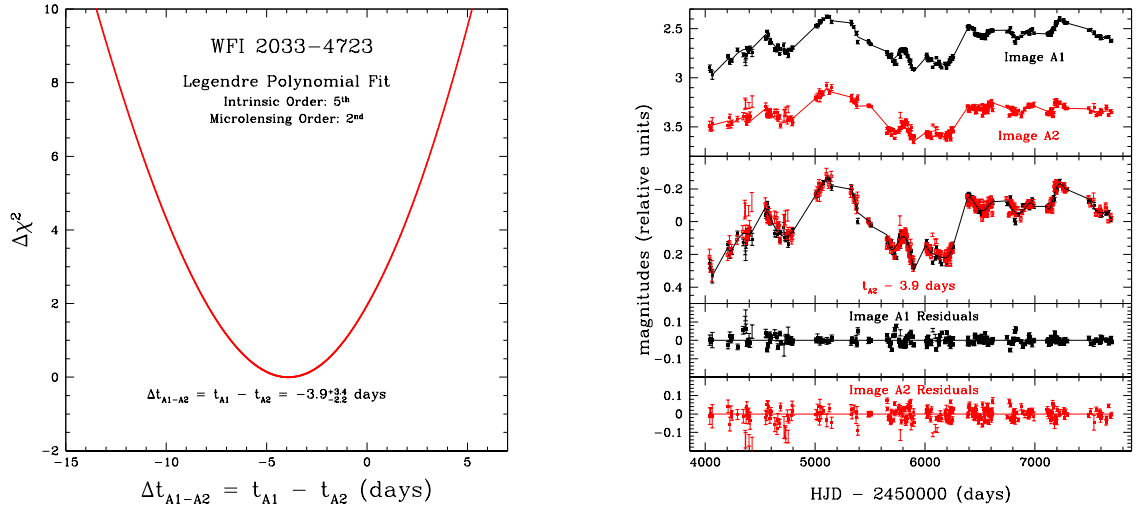

Fig. 5.— Left: χ^2 surfaces for our measurement of the time delay between images A1 and A2. Right: Top panel shows the raw light curves. Middle panel shows time-delay shifted and normalized light curves in which the 2$^{\rm nd}$ order polynomial fit to the microlensing variability has been removed. The solid line shows the 5$^{\rm th}$ order best fit to the intrinsic variability. Bottom panel shows residuals following subtraction of both the intrinsic and microlensing fits.

4.2. Monte Carlo Method

Armed with 400 sets of magnification patterns for a range of lens galaxy mass models, we used the Monte Carlo light curve fitting technique of Kochanek (2004) as modified by Morgan et al. (2008) to model unresolved image pairs. Since the light curves are a full 13 seasons in length, we binned them using a window of $\delta t_{bin} = 20$ days to reduce computation time. The twenty day binning window was sufficiently short to avoid overly smoothing the microlensing variability while adequately reducing the run time for the Monte Carlo routine. The date of each twenty-day bin was set as the mean Heliocentric Julian Date (HJD) of the measurements included in that bin. Since the light curves from V08 do not provide individual measurements for the A1 and A2 images, we adjusted the statistical weight of the A = A1+A2 data points to appropriately account for the combined fluxes in these cases. Also, for the combined cases we used either the A1 or A2 magnification pattern (with equal frequency) when creating a simulated light curve for the combined A1 + A2 image.

Prior to each Monte Carlo trial, we convolved each set of magnification patterns with a Gaussian surface brightness profile at a range of trial source sizes

$$14.5 \leq \log(\hat{r_s}\langle M_*/M_\odot\rangle^{-1/2}/\mathrm{cm}) \leq 18.0, \quad (1)$$

where $\hat{r_s}$ is the radius of the accretion disk scaled by $\langle M_*\rangle^{1/2}$, the mean mass of a lens galaxy star. Although we used a Gaussian profile, the exact choice of photometric emission model is unimportant, since Mortonson et al. (2005) showed that microlensing statistics are largely a function of the half-light radius of the emitting region, not the exact properties of the emission profile. In a given trial, a convolved pattern is run past a model point source on a random trajectory and at a random transverse speed 10 km/s $\leq (\hat{v}_e \langle M_*/M_\odot\rangle^{-1/2}) \leq 10^6$ km/s. Changes in magnification with time are logged at the epochs of the observed data and a running comparison with the light curves is made. The quality of the fit is tallied in real time using a χ^2 statistic, and, to save computational time, fits with $\chi^2/N_{dof} > 3.0$ are discarded since they will not contribute significantly to the Bayesian integrals in our post-run analysis. During the curve fitting process, we allowed for 0.07 and 0.03 magnitudes of systematic error in the photometry of images A1 & A2 and B & C, respectively. We also allowed for 0.5 magnitudes of uncertainty in the intrinsic flux ratios between the lensed images, since both the continuum and the broad line region are affected by microlensing in this lens (Motta et al. 2017) and to allow for the influence of substructure in the lens. We attempted 10^7 fits per set of magnification patterns for a grand total of $N_{\mathrm{trials}} = 4\times10^9$ trials, requiring approximately two weeks of run time on the US Naval Academy High Performance Computing (HPC) cluster. In Figure 6, we display two of the best fits from our Monte Carlo analysis to the time-delay corrected difference light curves of WFI2033. Consistent with the findings of Giannini et al. (2017), we easily see $\sim$ 0.2 mags of microlensing variability in

the difference light curves from image C. The microlensing in images A1, A2 and B is less pronounced, with $\lesssim 0.1$ mags of extrinsic variability over the 13 seasons of monitoring.

4.3. Bayesian Analysis of Monte Carlo Results

Using Bayes' theorem, the probability of the parameters given the data D is

$$P(\xi_p, \xi_t|D) \propto P(D|\xi_p, \xi_t)P(\xi_p)P(\xi_t), \tag{2}$$

where ξ_p is the collection of physical variables, ξ_t is the collection of trajectory variables and $P(\xi_t)$ and $P(\xi_p)$ are the prior probabilities for the trajectory and physical variables, respectively. The physical variables are parameters of the local magnification tensors (mean convergence κ and mean shear γ), the local properties of the stars (surface density of stars $\kappa_\star$, mass of the average microlens $\langle M_* \rangle$), the scale radius of the source r_s, and the effective velocity of the source $\vec{v}_e$. The probability distribution for any variable of interest can be obtained by marginalizing over the other variables of the simulation. For example, to find the probability density for the scale radius r_s,

$$P(r_s|D) \propto \int P(D|\vec{p}, r_s)P(\vec{p})P(r_s)d\vec{p} \tag{3}$$

where $P(D|\vec{p}, r_s)$ is the probability of fitting the data in a particular trial, $P(\vec{p})$ sets the priors on the microlensing variables ξ_p & ξ_t, and $P(r_s)$ is the (uniform) prior on the scale radius. The total probability is then normalized so that $\int P(r_s|D)dr_s = 1$.

We initially do the calculation in "Einstein units", where all lengths depend upon a factor of the unknown mean stellar mass, $\langle M_*/M_\odot \rangle^{1/2}$. For example, in Figure 8, we display the probability density for the accretion disk scale radius $\hat{r}_s = r_s \langle M_*/M_\odot \rangle^{-1/2}$ in Einstein Units in which the plotted values assume $M_* = 1.0 M_\odot$. This degeneracy can be broken, however, by examining Figure 7, where we display the probability density for the scaled effective velocity $\hat{v}_e = v_e \langle M_*/M_\odot \rangle^{-1/2}$ (Einstein Units) from the Monte Carlo simulation. We also display a model in physical units for the expected transverse velocity $dP(v_e)/d\log(v_e)$ which serves as the statistical prior on v_e. Since $\hat{v}_e = v_e \langle M_*/M_\odot \rangle^{-1/2}$, we convolve the prior on v_e with the probability density for $\hat{v}_e$ to produce a probability density for $\langle M_* \rangle$. The probability density for $\langle M_* \rangle$ is then used to convert all scaled lengths (e.g. $\hat{r}_s$) into true, physical units (e.g. r_s) by convolving $dP(M_*)/d\log(M_*)$ with the quantity of interest.

We construct the prior on the transverse velocity, $dP(v_e)/d\log(v_e)$, using the method described in Kochanek (2004). For the peculiar velocity components of both lens and source, we make redshift-based estimates from the models of Mosquera & Kochanek (2011). We

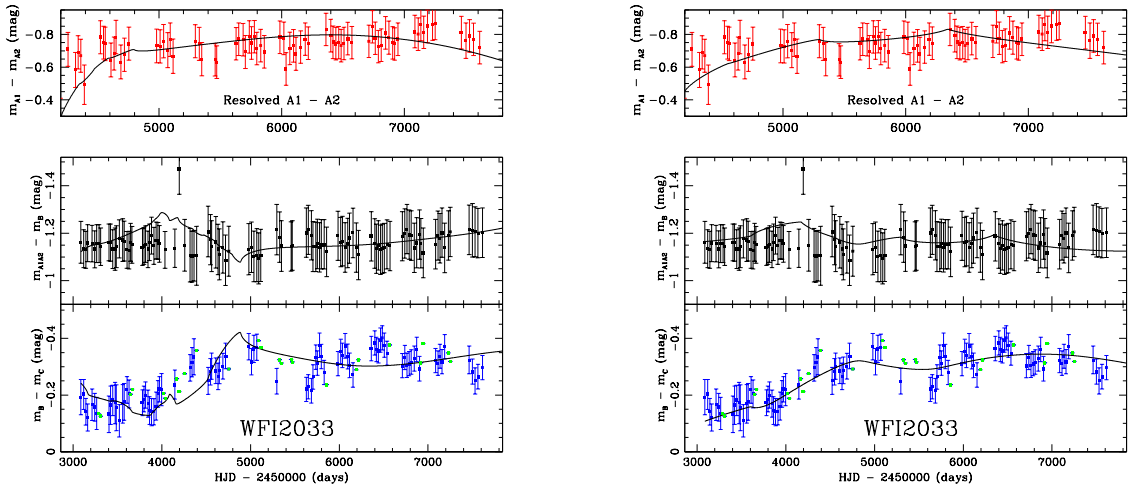

Fig. 6.— Examples of good fits from the Monte Carlo microlensing simulation to the time-delay corrected difference light curves of WFI2033. The fits were produced by the $f_{M/L} = 0.8$ (left panel) and $f_{M/L} = 0.4$ (right panel) models. Points labeled in green were not used in the analysis, as they required extrapolation of > 10 days into the inter-season gaps when shifting the light curves by the time delays. Note the $\gtrsim 0.2$ mags of extrinsic variability evident in the image B-C difference light curve.

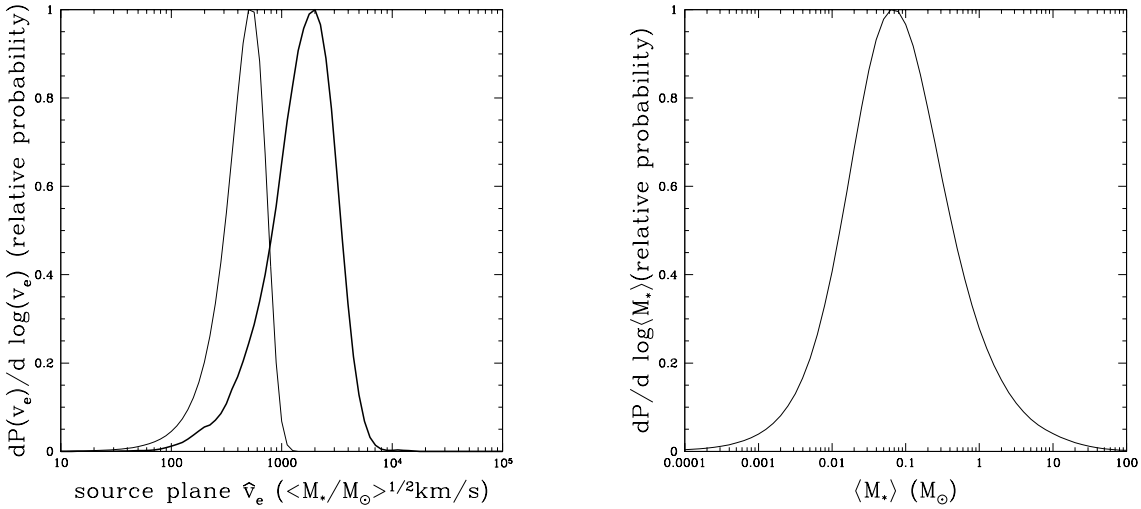

Fig. 7.— Left: Probability density for the effective source velocity $\hat{v}_e$ for WFI2033. The heavy curve is the scaled effective velocity distribution in Einstein units with median $\hat{v}_e = 1.5 \times 10^3 \, \langle M_*/M_\odot \rangle^{1/2} \mathrm{km\,s^{-1}}$. The thinner curve indicates the prior probability distribution for the true source velocity v_e, which we construct using the method described in Kochanek (2004). Right: The convolution of the prior on v_e with the probability density for $\hat{v}_e$ yields the probability density for $\langle M_* \rangle$, which we use to convert the source size measurement into physical units, independent of a prior on $\langle M_* \rangle$. Our estimate for the median lens galaxy stellar mass is $\langle M_*/M_\odot \rangle = 0.08^{+0.36}_{-0.05}$.

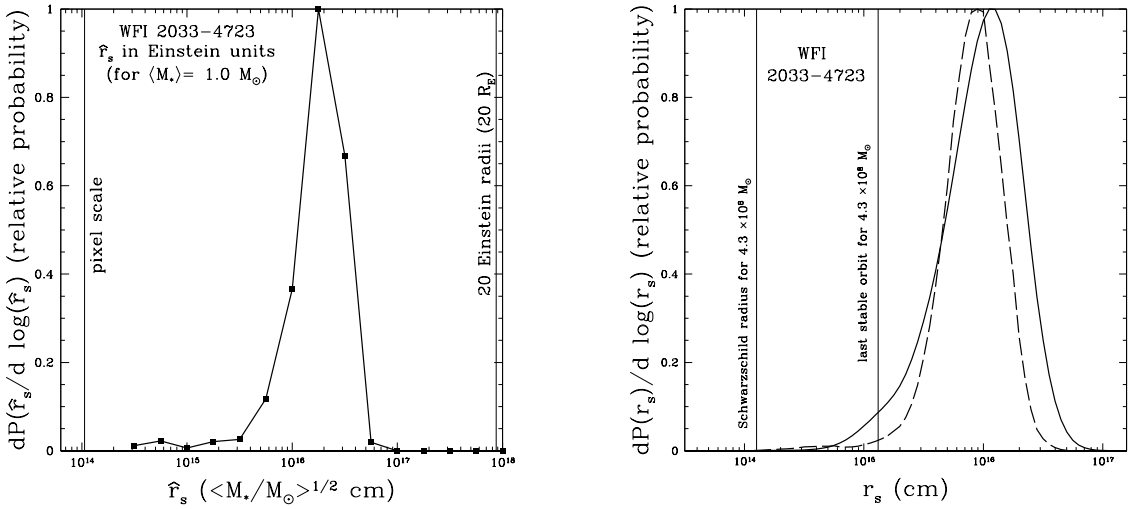

Fig. 8.— Left: Probability density for the Gaussian scale radius in Einstein units $\hat{r}_s = r_s\langle M_*/M_\odot\rangle^{-1/2}$. Right: Relative probability density for the thin disk scale radius r_s in physical units for WFI2033 at $\lambda_{rest} = 2632$ Å. The solid line represents the probability density arising from the microlensing simulations using the prior on the true effective velocity v_e, while the dotted line shows the result of imposing a uniform prior on the mean microlens mass of $0.1 < \langle M_*/M_\odot\rangle < 1.0$.

estimate the velocity dispersion of the lens galaxy from its Einstein radius, assuming the galaxy is a singular isothermal sphere with relaxed dynamics, which Treu & Koopmans (2004) and Bolton et al. (2008) show is a good approximation.

We display the probability density for the scale radius in physical units r_s in Figure 8. In this plot, we also show a probability density for r_s obtained by assuming a uniform prior on the median lens galaxy stellar mass of $0.1 \leq \langle M_*/M_\odot \rangle \leq 1.0$. A brief inspection of the plot reveals that the results without a prior on the microlens mass $\langle M_* \rangle$ are robustly consistent with the results using the uniform mass prior. As a final step we must correct the scale radius for the disk's inclination i by multiplying by $(\cos i)^{-1/2}$, which is necessary because we have assumed a face-on disk in our simulations and microlensing amplitudes depend on the projected area of a source rather than the shape. We adopt the measurement made without the mass prior $\log\left\{(r_s/\mathrm{cm})[\cos(i)/0.5]^{1/2}\right\} = 15.86^{+0.25}_{-0.27}$ at $\lambda_{rest} = 2481$Å, where i is the inclination angle.

5. RESULTS & DISCUSSION

In Figure 9, we plot the size of the accretion disk in WFI2033 on the Accretion Disk Size - Black Hole Mass Relation (Morgan et al. 2010) assuming an inclination angle $i = 60°$, where we have corrected the scale radius r_s at the wavelength corresponding to the center of the rest-frame R-band, $\lambda_{rest} = \lambda_{eff,R}/(1 + z_s) = 2481$ Å, to r_{2500}, the scale radius at $\lambda_{rest} = 2500$ Å, assuming the $r_s \propto \lambda^{4/3}$ scaling of Shakura & Sunyaev (1973) thin disk theory. We assume $\langle \cos(i) \rangle = 0.5$ or $\langle i \rangle = 60°$, the expectation value for the inclination of a randomly oriented disk. For the black hole mass (M_{BH}), we use the result from Sluse et al. (2012), who used the Mg II emission line to find $\log(M_{BH}/M_\odot) = 8.63 \pm 0.35$. Motta et al. (2017) also estimated M_{BH} in this system using Keplerian dynamics, but their method yielded very large uncertainties with $M_{BH-Motta17} = 1.2^{+3.1}_{-0.8} \times 10^8\,\mathrm{M}_\odot$. The Morgan et al. (2010) relation was derived using M_{BH} estimates based on emission line widths so the emission line width-based measurement from Sluse et al. (2012) is a better choice.

The expectation value for the scale radius at $\lambda_{rest} = 2681$Å without the prior on the mass of microlenses is $\log\left\{(r_s/\mathrm{cm})[\cos(i)/0.5]^{1/2}\right\} = 15.86^{+0.25}_{-0.27}$. This is fully consistent with the results of Motta et al. (2017), who estimate a scale radius $r_s \approx 1.6^{+0.5}_{-0.4} \times 10^{16}$ cm at $\lambda_{rest} = 1310$ Å using single-epoch spectroscopy, which, when scaled to 2481 Å assuming $r_s \propto \lambda^{4/3}$ is $\log(r_s/\mathrm{cm}) = 15.8^{+0.2}_{-0.1}$. The Motta et al. (2017) result is strongly dependent upon priors, especially the assumption of a median microlens mass $\langle M_*/M_\odot \rangle = 0.3$, nevertheless, the independence of the techniques provides robust support for our result. Blackburne et al. (2011) also estimated the scale radius of the accretion disk in WFI2033 using single epoch,

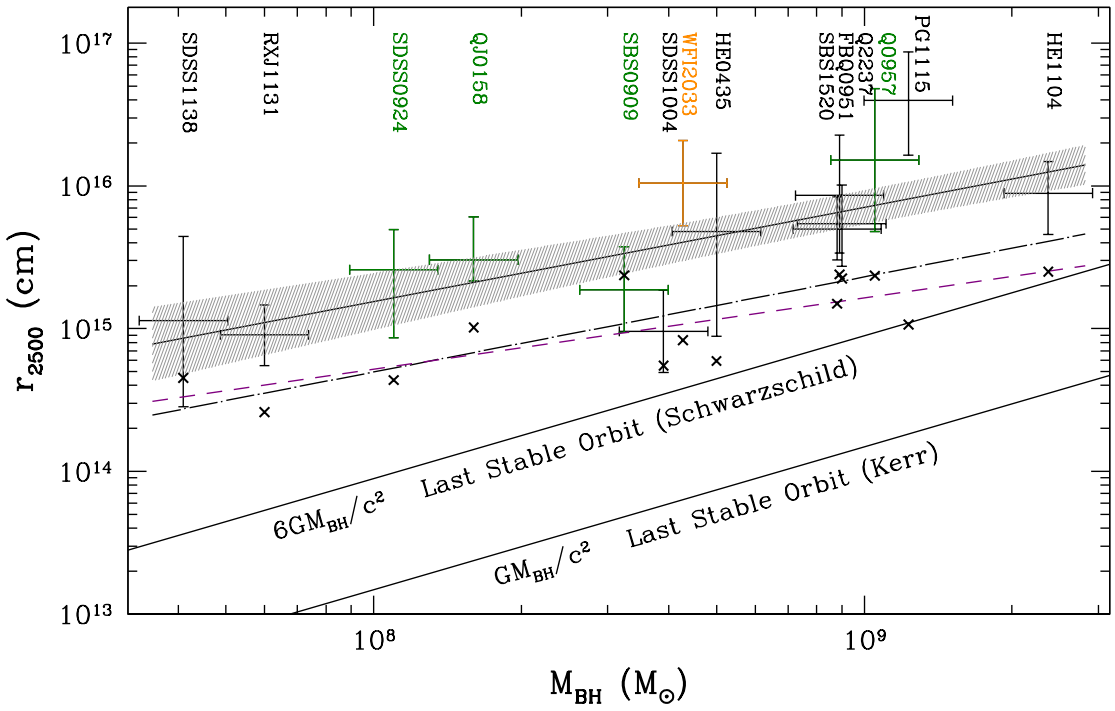

Fig. 9.— Accretion disk size versus supermassive black hole mass relation (thick solid line) and data from Morgan et al. (2010) with new measurements of r_s for Q 0957+561 (Hainline et al. 2012), QJ 0158–4723 (Morgan et al. 2012), SBS 0909+532 (Hainline et al. 2013) and SDSS 0924+0219 (MacLeod et al. 2015) (plotted in green) and WFI2033 (plotted in orange), all scaled to 2500 Å and corrected to 60° inclination. The dash-shaded region indicates the 1σ boundaries from uncertainties in the slope and intercept. The black dot-dashed line shows the scale radius as a function of central black hole mass predicted by theoretical thin disk models (for $L/L_E = 1/3$ and $\eta = 0.1$), while the small diagonal crosses indicate the thin disk size predicted by the magnification-corrected luminosity of the different quasars. The dashed purple line is a fit to the luminosity-based thin disk size estimates (diagonal crosses). The microlensing source size for WFI2033 is larger than the luminosity-constrained thin disk size and the theoretical thin disk size based on black hole mass, similar to the findings of Pooley et al. (2007), Morgan et al. (2010) and Mediavilla et al. (2011).

multi-wavelength photometry, but their results are, by their own admission, anomalous, as they also predict with highest likelihood an accretion disk with an inverted (increasing toward the outer edge) temperature profile. Like Motta et al. (2017), our size measurement is significantly smaller than the Blackburne et al. (2011) estimate.

In Figure 9, we made several updates in addition to the new WFI2033 measurement. Measurements of the accretion disk scale radius using the microlensing variability technique of Q 0957+561 (Hainline et al. 2012), SBS 0909+532 (Hainline et al. 2013) were added, and updates to the QJ 0158–4723 (Morgan et al. 2012), and SDSS 0924+0219 (MacLeod et al. 2015) measurements were also included. With changes to 2 out of the 11 existing points and the addition of 3 new measurements, the updated Accretion Disk Size - Black Hole Mass Relation (Morgan et al. 2010) is

$$\log(r_{2500}/\mathrm{cm}) = (15.85 \pm 0.12) + (0.66 \pm 0.15)\log(M_{BH}/10^9\mathrm{M}_\odot). \quad (4)$$

This is consistent with the original fit from Morgan et al. (2010), $\log(R_{2500}/\mathrm{cm}) = (15.78 \pm 0.12) + (0.80 \pm 0.17)\log(M_{BH}/10^9\mathrm{M}_\odot)$, and the shallower slope brings the relation into excellent agreement with the expectation from thin disk theory ($r_s \propto M_{BH}^{2/3}$).

There are now 14 systems in which the accretion disk size has been measured using the microlensing variability (e.g. Kochanek 2004) technique. With the exception of SBS 0909+532, in which the luminosity-based size estimate is marginally larger than the microlensing-based size measurement, microlensing-based size measurements are consistently larger than the luminosity-based thin disk size estimates by an average of ~ 0.55 dex. The SBS 0909+532 luminosity-based thin disk size estimate is somewhat suspect, however, since Sluse et al. (2012) and Lehár et al. (2000) found very different photometric fits for the lens galaxy in this system, leading to significant uncertainty in the magnification and, consequently, the intrinsic luminosity. Very recent continuum emission region reverberation mapping studies in local, lower luminosity AGN (e.g. Fasnaugh et al. 2018; Edelson et al. 2017; McHardy et al. 2016) have revealed similar discrepancies between observed accretion disk size measurements and the predictions of thin disk theory. In Morgan et al. (2010), we proposed that real accretion disks lack the necessary surface brightness to produce their observed luminosity from the smaller area of a simple thin disk model, and we remain confident in that conclusion. We were nevertheless intrigued to find that the slope of r_s vs M_{BH} is remarkably consistent with the predictions of thin disk theory ($r_s \propto M_{BH}^{2/3}$), so it is the intercept in the accretion disk-size black hole mass relation that is inconsistent with thin disk theory, rather than the slope. In Morgan et al. (2010), we suggested that the most promising explanation for the discrepancy is that accretion disks may have shallower temperature slopes than that predicted by thin disk theory $T(r) \propto r^{3/4}$, and this hypothesis remains fully viable. We are hopeful that our ongoing lensed quasar monitoring campaign

in the infrared ($J-$, $H-$ and $K-$band), corresponding to optical emission in the rest frame, will allow for measurements of accretion disk temperature profiles in the near future.

This material is based upon work supported by the National Science Foundation under grant AST-1614018 to C.W.M. and grants AST-1515876 & AST-1814440 to C.S.K. $COSMOGRAIL$ is made possible thanks to the continuous work of all observers and technical staff obtaining the monitoring observations, in particular at the Swiss Leonhard Euler telescope at La Silla Observatory, which is supported by the Swiss National Science Foundation. V. Bonvin and F. Courbin are also supported by the Swiss National Science Foundation (SNSF). This work is partly based on observations obtained with the Small and Moderate Aperture Research Telescope System (SMARTS) 1.3m, which is operated by the SMARTS Consortium. Thanks to V. Motta for helpful discussions about black hole masses and to R. Witt for many hours of help with the USNA High Performance Computing Cluster.

Table 3. WFI2033–4723 Light Curves - SMARTS

HJD	A1	A2	B	C	χ^2/N_{dof}	Source
3082.897	2.747 ± 0.012	3.396 ± 0.021	3.425 ± 0.012	3.640 ± 0.015	1.6	SMARTS
3112.857	2.769 ± 0.017	3.411 ± 0.029	3.554 ± 0.014	3.638 ± 0.017	1.7	SMARTS
3138.866	2.835 ± 0.017	3.460 ± 0.030	3.610 ± 0.016	3.708 ± 0.019	3.0	SMARTS
3146.900	2.848 ± 0.015	3.448 ± 0.025	3.606 ± 0.013	3.718 ± 0.015	5.7	SMARTS
3154.840	2.870 ± 0.015	3.511 ± 0.025	3.635 ± 0.013	3.670 ± 0.015	2.9	SMARTS
3175.825	2.937 ± 0.011	3.502 ± 0.016	3.584 ± 0.011	3.751 ± 0.013	6.0	SMARTS
3184.777	2.948 ± 0.014	3.519 ± 0.023	3.601 ± 0.013	3.748 ± 0.016	1.8	SMARTS
3211.740	2.921 ± 0.014	3.572 ± 0.025	3.568 ± 0.013	3.737 ± 0.016	1.7	SMARTS
3282.634	2.996 ± 0.014	3.444 ± 0.020	3.544 ± 0.011	3.780 ± 0.014	3.0	SMARTS
3295.616	2.892 ± 0.013	3.566 ± 0.023	3.544 ± 0.012	3.794 ± 0.015	4.2	SMARTS
3298.566	2.931 ± 0.015	3.548 ± 0.025	3.564 ± 0.014	3.787 ± 0.017	1.4	SMARTS
3310.551	2.881 ± 0.013	3.578 ± 0.024	3.605 ± 0.013	3.789 ± 0.015	1.5	SMARTS
3320.551	3.081 ± 0.021	3.273 ± 0.024	3.602 ± 0.015	3.831 ± 0.019	4.0	SMARTS
3592.759	2.966 ± 0.016	3.607 ± 0.028	3.528 ± 0.014	3.890 ± 0.019	1.8	SMARTS
3625.668	2.881 ± 0.014	3.531 ± 0.024	3.463 ± 0.015	3.854 ± 0.022	1.5	SMARTS
3651.552	2.838 ± 0.017	3.475 ± 0.030	3.423 ± 0.013	3.824 ± 0.021	2.0	SMARTS
3661.571	2.893 ± 0.031	3.339 ± 0.045	3.445 ± 0.024	3.875 ± 0.038	1.0	SMARTS
3665.553	2.904 ± 0.017	3.363 ± 0.024	3.440 ± 0.013	3.801 ± 0.018	2.1	SMARTS
3675.522	2.895 ± 0.018	3.315 ± 0.025	3.411 ± 0.015	3.800 ± 0.020	2.2	SMARTS
3826.891	2.762 ± 0.018	3.483 ± 0.034	3.436 ± 0.016	3.681 ± 0.020	1.0	SMARTS
3832.855	2.742 ± 0.024	3.453 ± 0.045	3.553 ± 0.020	3.723 ± 0.026	4.0	SMARTS
3852.870	2.740 ± 0.015	3.495 ± 0.028	3.524 ± 0.015	3.697 ± 0.018	1.9	SMARTS
3863.788	2.736 ± 0.016	3.471 ± 0.030	3.570 ± 0.018	3.679 ± 0.020	4.7	SMARTS
3886.859	2.819 ± 0.012	3.486 ± 0.020	3.599 ± 0.014	3.666 ± 0.015	1.8	SMARTS
3937.732	2.942 ± 0.016	3.578 ± 0.028	3.517 ± 0.014	3.772 ± 0.018	1.6	SMARTS
3994.640	2.938 ± 0.019	3.281 ± 0.025	3.499 ± 0.014	3.785 ± 0.019	2.3	SMARTS
4021.575	2.932 ± 0.018	3.325 ± 0.027	3.598 ± 0.016	3.757 ± 0.020	1.5	SMARTS
4042.528	2.889 ± 0.027	3.478 ± 0.046	3.532 ± 0.025	3.738 ± 0.032	0.9	SMARTS
4050.555	2.921 ± 0.016	3.510 ± 0.026	3.494 ± 0.015	3.765 ± 0.018	4.4	SMARTS
4064.511	2.963 ± 0.041	3.462 ± 0.064	3.397 ± 0.036	3.728 ± 0.050	0.6	SMARTS
4207.876	2.773 ± 0.019	3.472 ± 0.036	3.540 ± 0.016	3.791 ± 0.022	3.5	SMARTS
4224.867	2.832 ± 0.023	3.400 ± 0.038	3.456 ± 0.020	3.763 ± 0.028	1.8	SMARTS
4234.918	2.811 ± 0.018	3.471 ± 0.031	3.374 ± 0.014	3.695 ± 0.020	0.9	SMARTS
4243.898	2.818 ± 0.015	3.450 ± 0.026	3.385 ± 0.013	3.713 ± 0.018	1.3	SMARTS
4293.829	2.703 ± 0.015	3.413 ± 0.028	3.399 ± 0.013	3.649 ± 0.017	1.3	SMARTS
4345.711	2.758 ± 0.021	3.381 ± 0.036	3.353 ± 0.016	3.700 ± 0.023	2.1	SMARTS
4363.622	2.796 ± 0.038	3.255 ± 0.057	3.304 ± 0.031	3.703 ± 0.048	0.3	SMARTS
4367.667	2.839 ± 0.030	3.259 ± 0.042	3.345 ± 0.024	3.675 ± 0.035	0.9	SMARTS
4371.624	2.768 ± 0.024	3.395 ± 0.043	3.357 ± 0.020	3.685 ± 0.029	0.8	SMARTS
4378.583	2.687 ± 0.014	3.449 ± 0.026	3.343 ± 0.012	3.680 ± 0.017	1.7	SMARTS
4387.542	2.690 ± 0.014	3.414 ± 0.026	3.343 ± 0.013	3.659 ± 0.017	1.6	SMARTS
4390.519	2.706 ± 0.012	3.407 ± 0.021	3.324 ± 0.012	3.648 ± 0.016	1.8	SMARTS
4394.534	2.696 ± 0.023	3.404 ± 0.043	3.311 ± 0.021	3.719 ± 0.031	0.9	SMARTS
4397.544	2.725 ± 0.020	3.276 ± 0.032	3.271 ± 0.017	3.697 ± 0.025	1.0	SMARTS
4407.520	2.693 ± 0.025	3.384 ± 0.046	3.257 ± 0.018	3.661 ± 0.028	1.0	SMARTS
4427.512	2.739 ± 0.037	3.233 ± 0.057	3.322 ± 0.032	3.680 ± 0.047	0.7	SMARTS

Table 3—Continued

HJD	A1	A2	B	C	χ^2/N_{dof}	Source
4550.907	2.589 ± 0.021	3.286 ± 0.039	3.349 ± 0.020	3.630 ± 0.028	3.8	SMARTS
4557.869	2.587 ± 0.013	3.304 ± 0.024	3.321 ± 0.012	3.623 ± 0.016	1.4	SMARTS
4564.904	2.519 ± 0.011	3.373 ± 0.021	3.339 ± 0.011	3.618 ± 0.014	3.0	SMARTS
4571.811	2.554 ± 0.015	3.369 ± 0.031	3.346 ± 0.013	3.569 ± 0.017	1.2	SMARTS
4588.916	2.637 ± 0.015	3.331 ± 0.027	3.373 ± 0.013	3.602 ± 0.017	2.5	SMARTS
4589.840	2.603 ± 0.014	3.354 ± 0.025	3.385 ± 0.012	3.570 ± 0.015	4.4	SMARTS
4596.807	2.637 ± 0.012	3.379 ± 0.022	3.393 ± 0.011	3.587 ± 0.014	1.7	SMARTS
4633.820	2.704 ± 0.021	3.350 ± 0.037	3.374 ± 0.017	3.703 ± 0.026	2.6	SMARTS
4653.812	2.706 ± 0.020	3.350 ± 0.036	3.379 ± 0.016	3.658 ± 0.023	0.9	SMARTS
4660.793	2.660 ± 0.015	3.403 ± 0.029	3.392 ± 0.013	3.677 ± 0.019	1.6	SMARTS
4678.731	2.744 ± 0.013	3.391 ± 0.022	3.376 ± 0.011	3.681 ± 0.015	4.4	SMARTS
4684.695	2.698 ± 0.012	3.482 ± 0.022	3.378 ± 0.011	3.630 ± 0.015	2.6	SMARTS
4716.731	2.667 ± 0.031	3.375 ± 0.058	3.363 ± 0.026	3.690 ± 0.038	0.6	SMARTS
4724.697	2.725 ± 0.020	3.348 ± 0.035	3.328 ± 0.019	3.676 ± 0.026	1.8	SMARTS
4732.649	2.729 ± 0.025	3.331 ± 0.042	3.324 ± 0.019	3.684 ± 0.027	1.2	SMARTS
4747.635	2.729 ± 0.017	3.432 ± 0.032	3.388 ± 0.014	3.691 ± 0.019	1.2	SMARTS
4754.586	2.765 ± 0.022	3.314 ± 0.036	3.379 ± 0.018	3.659 ± 0.024	0.5	SMARTS
4758.587	2.703 ± 0.012	3.408 ± 0.022	3.359 ± 0.011	3.671 ± 0.014	3.7	SMARTS
4783.521	2.705 ± 0.016	3.410 ± 0.029	3.349 ± 0.016	3.651 ± 0.021	1.0	SMARTS
4790.543	2.682 ± 0.012	3.456 ± 0.023	3.339 ± 0.011	3.690 ± 0.015	3.4	SMARTS
4797.550	2.686 ± 0.014	3.422 ± 0.026	3.366 ± 0.012	3.686 ± 0.015	2.2	SMARTS
5009.684	2.463 ± 0.014	3.193 ± 0.026	3.135 ± 0.011	3.551 ± 0.016	4.5	SMARTS
5021.762	2.461 ± 0.022	3.191 ± 0.043	2.993 ± 0.020	3.407 ± 0.031	1.1	SMARTS
5038.667	2.430 ± 0.014	3.130 ± 0.025	3.071 ± 0.010	3.549 ± 0.016	4.8	SMARTS
5043.671	2.421 ± 0.021	3.196 ± 0.042	3.023 ± 0.022	3.478 ± 0.035	0.5	SMARTS
5053.723	2.417 ± 0.016	3.153 ± 0.030	2.987 ± 0.012	3.480 ± 0.020	1.7	SMARTS
5072.652	2.393 ± 0.011	3.151 ± 0.021	3.020 ± 0.010	3.433 ± 0.015	1.8	SMARTS
5106.592	2.370 ± 0.019	3.074 ± 0.035	3.038 ± 0.015	3.415 ± 0.022	1.2	SMARTS
5127.553	2.372 ± 0.012	3.140 ± 0.022	3.092 ± 0.011	3.379 ± 0.014	2.6	SMARTS
5150.518	2.423 ± 0.017	3.090 ± 0.031	3.130 ± 0.013	3.421 ± 0.018	2.1	SMARTS
5326.806	2.420 ± 0.014	3.212 ± 0.028	3.232 ± 0.012	3.443 ± 0.016	1.3	SMARTS
5335.836	2.449 ± 0.013	3.183 ± 0.023	3.236 ± 0.012	3.483 ± 0.015	2.1	SMARTS
5353.802	2.473 ± 0.010	3.237 ± 0.019	3.271 ± 0.011	3.445 ± 0.012	2.9	SMARTS
5372.779	2.542 ± 0.017	3.229 ± 0.032	3.254 ± 0.017	3.514 ± 0.023	0.5	SMARTS
5379.848	2.533 ± 0.016	3.272 ± 0.030	3.280 ± 0.014	3.503 ± 0.018	1.0	SMARTS
5388.792	2.627 ± 0.017	3.193 ± 0.027	3.152 ± 0.011	3.601 ± 0.018	7.8	SMARTS
6407.908	2.534 ± 0.021	3.311 ± 0.041	3.103 ± 0.017	3.546 ± 0.026	2.8	SMARTS
6418.889	2.511 ± 0.012	3.257 ± 0.021	3.136 ± 0.011	3.635 ± 0.015	5.1	SMARTS
6431.908	2.498 ± 0.014	3.225 ± 0.027	3.123 ± 0.011	3.659 ± 0.018	8.7	SMARTS
6436.834	2.496 ± 0.017	3.298 ± 0.035	3.177 ± 0.016	3.627 ± 0.025	1.8	SMARTS
6458.851	2.546 ± 0.013	3.336 ± 0.025	3.180 ± 0.011	3.559 ± 0.015	4.1	SMARTS
6464.838	2.534 ± 0.017	3.373 ± 0.035	3.053 ± 0.014	3.578 ± 0.023	11.8	SMARTS
6488.762	2.620 ± 0.017	3.276 ± 0.030	3.230 ± 0.013	3.578 ± 0.018	2.4	SMARTS
6492.691	2.587 ± 0.017	3.282 ± 0.030	3.186 ± 0.014	3.598 ± 0.022	5.0	SMARTS
6508.687	2.589 ± 0.045	3.311 ± 0.088	3.142 ± 0.036	3.606 ± 0.060	0.9	SMARTS
6760.883	2.546 ± 0.016	3.251 ± 0.030	3.212 ± 0.014	3.589 ± 0.020	3.3	SMARTS

Table 3—Continued

HJD	A1	A2	B	C	χ^2/N_{dof}	Source
6825.834	2.594 ± 0.024	3.401 ± 0.049	3.289 ± 0.019	3.632 ± 0.029	1.2	SMARTS
6857.805	2.589 ± 0.017	3.367 ± 0.033	3.179 ± 0.012	3.665 ± 0.020	3.2	SMARTS
6944.600	2.546 ± 0.016	3.309 ± 0.031	3.131 ± 0.011	3.596 ± 0.017	4.9	SMARTS
7141.898	2.541 ± 0.014	3.320 ± 0.026	3.153 ± 0.012	3.622 ± 0.018	2.5	SMARTS
7150.873	2.607 ± 0.033	3.209 ± 0.057	3.149 ± 0.027	3.683 ± 0.048	2.1	SMARTS
7253.669	2.420 ± 0.013	3.237 ± 0.026	3.245 ± 0.012	3.503 ± 0.016	2.3	SMARTS
7255.638	2.406 ± 0.023	3.228 ± 0.047	3.274 ± 0.021	3.503 ± 0.030	0.7	SMARTS
7269.616	2.339 ± 0.014	3.304 ± 0.032	3.267 ± 0.013	3.577 ± 0.019	3.7	SMARTS
7278.583	2.458 ± 0.014	3.275 ± 0.028	3.266 ± 0.013	3.519 ± 0.018	2.0	SMARTS
7340.526	2.459 ± 0.012	3.374 ± 0.025	3.225 ± 0.012	3.556 ± 0.016	1.7	SMARTS
7344.525	2.509 ± 0.023	3.241 ± 0.044	3.222 ± 0.024	3.630 ± 0.036	0.9	SMARTS
7598.716	2.611 ± 0.021	3.338 ± 0.040	3.341 ± 0.020	3.605 ± 0.027	0.6	SMARTS
7603.680	2.619 ± 0.015	3.355 ± 0.027	3.364 ± 0.012	3.607 ± 0.017	1.5	SMARTS
7605.790	2.586 ± 0.015	3.347 ± 0.028	3.319 ± 0.013	3.633 ± 0.017	4.1	SMARTS
7608.765	2.620 ± 0.017	3.323 ± 0.031	3.289 ± 0.013	3.636 ± 0.019	1.1	SMARTS
7613.738	2.583 ± 0.018	3.406 ± 0.037	3.317 ± 0.016	3.614 ± 0.022	1.1	SMARTS
7652.639	2.665 ± 0.020	3.274 ± 0.033	3.211 ± 0.015	3.462 ± 0.020	7.7	SMARTS
7661.601	2.634 ± 0.019	3.272 ± 0.032	3.320 ± 0.014	3.547 ± 0.020	2.3	SMARTS
7695.556	2.662 ± 0.017	3.344 ± 0.031	3.231 ± 0.013	3.587 ± 0.020	3.1	SMARTS
7702.583	2.610 ± 0.019	3.373 ± 0.038	3.302 ± 0.018	3.547 ± 0.023	2.4	SMARTS
7856.868	2.866 ± 0.032	3.130 ± 0.038	3.531 ± 0.026	3.762 ± 0.035	1.0	SMARTS
7867.882	2.676 ± 0.015	3.471 ± 0.029	3.536 ± 0.015	3.691 ± 0.018	2.5	SMARTS
7872.884	2.687 ± 0.014	3.478 ± 0.027	3.452 ± 0.014	3.736 ± 0.019	2.1	SMARTS
7877.840	2.700 ± 0.017	3.516 ± 0.034	3.497 ± 0.017	3.701 ± 0.022	1.6	SMARTS
7894.808	2.717 ± 0.020	3.462 ± 0.038	3.511 ± 0.018	3.723 ± 0.023	3.4	SMARTS
7904.766	2.697 ± 0.016	3.493 ± 0.031	3.520 ± 0.016	3.714 ± 0.020	4.4	SMARTS
7914.785	2.725 ± 0.024	3.372 ± 0.041	3.499 ± 0.027	3.756 ± 0.035	0.7	SMARTS

Note. — HJD is the Heliocentric Julian Day –2450000 days. The goodness of fit of the image, χ^2/N_{dof}, is used to rescale the formal uncertainties by a factor of $(\chi^2/N_{dof})^{1/2}$. The Image A1-C columns give the magnitudes of the quasar images relative to the comparison stars.

Table 4. WFI2033–4723 Light Curves - EULER

HJD	A1	A2	B	C	χ^2/N_{dof}	Source
5485.659	2.628 ± 0.008	3.285 ± 0.013	3.348 ± 0.007	3.597 ± 0.009	2.4	EULER
5488.637	2.644 ± 0.008	3.281 ± 0.013	3.341 ± 0.007	3.579 ± 0.008	3.8	EULER
5503.592	2.654 ± 0.006	3.294 ± 0.009	3.368 ± 0.005	3.615 ± 0.006	10.5	EULER
5506.571	2.662 ± 0.007	3.293 ± 0.010	3.378 ± 0.006	3.629 ± 0.007	6.3	EULER
5655.905	2.764 ± 0.002	3.518 ± 0.004	3.505 ± 0.003	3.684 ± 0.004	2.8	EULER
5656.910	2.742 ± 0.007	3.564 ± 0.013	3.499 ± 0.007	3.697 ± 0.008	6.1	EULER
5667.908	2.768 ± 0.001	3.506 ± 0.002	3.589 ± 0.002	3.732 ± 0.002	6.6	EULER
5674.897	2.792 ± 0.008	3.534 ± 0.014	3.569 ± 0.008	3.729 ± 0.009	2.2	EULER
5678.879	2.772 ± 0.007	3.528 ± 0.012	3.575 ± 0.006	3.733 ± 0.007	7.8	EULER
5682.896	2.773 ± 0.007	3.541 ± 0.012	3.587 ± 0.007	3.731 ± 0.008	5.7	EULER
5686.849	2.791 ± 0.007	3.518 ± 0.012	3.583 ± 0.007	3.742 ± 0.008	3.4	EULER
5694.851	2.760 ± 0.007	3.587 ± 0.012	3.602 ± 0.007	3.744 ± 0.008	11.0	EULER
5712.864	2.832 ± 0.006	3.536 ± 0.009	3.524 ± 0.006	3.829 ± 0.007	8.7	EULER
5723.776	2.860 ± 0.008	3.565 ± 0.013	3.495 ± 0.007	3.786 ± 0.009	2.6	EULER
5725.771	2.828 ± 0.002	3.616 ± 0.005	3.500 ± 0.004	3.784 ± 0.005	3.7	EULER
5739.722	2.861 ± 0.009	3.554 ± 0.016	3.431 ± 0.007	3.799 ± 0.009	2.5	EULER
5762.714	2.758 ± 0.008	3.549 ± 0.016	3.437 ± 0.008	3.792 ± 0.011	3.1	EULER
5766.821	2.746 ± 0.009	3.510 ± 0.016	3.387 ± 0.006	3.865 ± 0.010	3.4	EULER
5770.741	2.723 ± 0.007	3.534 ± 0.013	3.430 ± 0.006	3.807 ± 0.009	3.7	EULER
5775.621	2.785 ± 0.016	3.381 ± 0.028	3.449 ± 0.013	3.791 ± 0.018	1.1	EULER
5779.607	2.710 ± 0.007	3.515 ± 0.013	3.431 ± 0.006	3.783 ± 0.008	3.4	EULER
5783.712	2.725 ± 0.007	3.448 ± 0.013	3.414 ± 0.008	3.824 ± 0.011	2.8	EULER
5794.685	2.704 ± 0.006	3.473 ± 0.011	3.430 ± 0.006	3.805 ± 0.008	4.5	EULER
5804.569	2.712 ± 0.008	3.503 ± 0.015	3.501 ± 0.007	3.716 ± 0.009	2.9	EULER
5807.536	2.711 ± 0.001	3.500 ± 0.002	3.501 ± 0.002	3.720 ± 0.002	4.5	EULER
5815.552	2.702 ± 0.008	3.500 ± 0.015	3.528 ± 0.009	3.808 ± 0.011	4.9	EULER
5818.636	2.732 ± 0.007	3.454 ± 0.011	3.493 ± 0.007	3.803 ± 0.009	5.3	EULER
5820.656	2.741 ± 0.007	3.452 ± 0.011	3.500 ± 0.007	3.803 ± 0.009	5.0	EULER
5824.700	2.755 ± 0.009	3.432 ± 0.015	3.507 ± 0.007	3.798 ± 0.009	4.5	EULER
5827.557	2.715 ± 0.008	3.438 ± 0.013	3.575 ± 0.007	3.835 ± 0.010	8.9	EULER
5831.537	2.748 ± 0.005	3.464 ± 0.008	3.545 ± 0.006	3.773 ± 0.007	16.3	EULER
5839.610	2.783 ± 0.011	3.467 ± 0.020	3.545 ± 0.009	3.851 ± 0.013	3.4	EULER
5842.521	2.775 ± 0.009	3.536 ± 0.016	3.583 ± 0.009	3.805 ± 0.012	2.7	EULER
5854.529	2.813 ± 0.008	3.544 ± 0.014	3.585 ± 0.007	3.794 ± 0.009	4.1	EULER
5857.517	2.830 ± 0.007	3.580 ± 0.013	3.576 ± 0.006	3.763 ± 0.008	3.2	EULER
5865.500	2.849 ± 0.018	3.579 ± 0.034	3.608 ± 0.019	3.799 ± 0.024	0.9	EULER
5865.512	2.852 ± 0.009	3.534 ± 0.015	3.577 ± 0.008	3.785 ± 0.010	2.8	EULER
5869.535	2.819 ± 0.009	3.617 ± 0.017	3.583 ± 0.008	3.777 ± 0.010	2.5	EULER
5873.574	2.884 ± 0.017	3.509 ± 0.030	3.563 ± 0.013	3.847 ± 0.019	1.3	EULER
5887.557	2.916 ± 0.007	3.587 ± 0.013	3.542 ± 0.007	3.816 ± 0.008	3.2	EULER
5896.532	2.907 ± 0.010	3.653 ± 0.019	3.548 ± 0.009	3.810 ± 0.011	1.5	EULER
5897.530	2.912 ± 0.011	3.600 ± 0.020	3.525 ± 0.009	3.841 ± 0.012	2.4	EULER
6011.897	2.783 ± 0.001	3.567 ± 0.001	3.540 ± 0.001	3.775 ± 0.001	5.0	EULER
6015.909	2.759 ± 0.009	3.585 ± 0.019	3.602 ± 0.009	3.758 ± 0.011	7.1	EULER
6017.894	2.778 ± 0.007	3.558 ± 0.013	3.561 ± 0.007	3.757 ± 0.008	8.2	EULER
6018.905	2.808 ± 0.008	3.554 ± 0.015	3.550 ± 0.007	3.763 ± 0.009	2.3	EULER

Table 4—Continued

HJD	A1	A2	B	C	χ^2/N_{dof}	Source
6023.906	2.796 ± 0.009	3.601 ± 0.018	3.597 ± 0.009	3.780 ± 0.011	4.9	EULER
6028.900	2.822 ± 0.007	3.581 ± 0.012	3.589 ± 0.007	3.826 ± 0.009	4.8	EULER
6029.911	2.828 ± 0.009	3.587 ± 0.016	3.585 ± 0.008	3.812 ± 0.010	2.4	EULER
6047.869	2.811 ± 0.008	3.596 ± 0.015	3.588 ± 0.007	3.829 ± 0.009	7.3	EULER
6050.863	2.821 ± 0.008	3.559 ± 0.014	3.581 ± 0.007	3.865 ± 0.009	6.6	EULER
6058.888	2.810 ± 0.008	3.617 ± 0.014	3.565 ± 0.007	3.914 ± 0.011	4.9	EULER
6070.935	2.891 ± 0.007	3.480 ± 0.010	3.496 ± 0.007	3.897 ± 0.009	9.5	EULER
6092.942	2.864 ± 0.011	3.522 ± 0.019	3.516 ± 0.008	3.878 ± 0.012	3.6	EULER
6102.712	2.797 ± 0.007	3.577 ± 0.012	3.622 ± 0.007	3.891 ± 0.008	8.5	EULER
6109.823	2.854 ± 0.008	3.515 ± 0.013	3.575 ± 0.008	3.929 ± 0.010	7.4	EULER
6125.707	2.830 ± 0.008	3.577 ± 0.015	3.649 ± 0.007	3.902 ± 0.010	6.0	EULER
6129.706	2.857 ± 0.008	3.579 ± 0.015	3.632 ± 0.009	3.894 ± 0.012	5.8	EULER
6138.590	2.882 ± 0.011	3.600 ± 0.020	3.673 ± 0.010	3.865 ± 0.013	3.3	EULER
6151.591	2.899 ± 0.009	3.581 ± 0.017	3.630 ± 0.008	3.893 ± 0.010	2.7	EULER
6185.503	2.854 ± 0.012	3.592 ± 0.021	3.569 ± 0.012	3.942 ± 0.016	3.0	EULER
6185.515	2.855 ± 0.007	3.616 ± 0.011	3.567 ± 0.007	3.930 ± 0.009	7.4	EULER
6190.528	2.867 ± 0.007	3.591 ± 0.013	3.548 ± 0.007	3.940 ± 0.009	6.8	EULER
6194.537	2.864 ± 0.013	3.623 ± 0.025	3.533 ± 0.011	3.919 ± 0.018	1.3	EULER
6195.693	2.901 ± 0.007	3.562 ± 0.013	3.466 ± 0.007	3.914 ± 0.011	3.7	EULER
6217.615	2.860 ± 0.008	3.545 ± 0.014	3.405 ± 0.006	3.925 ± 0.009	6.2	EULER
6221.532	2.845 ± 0.009	3.566 ± 0.015	3.441 ± 0.007	3.931 ± 0.010	3.0	EULER
6224.554	2.819 ± 0.011	3.594 ± 0.022	3.439 ± 0.010	3.915 ± 0.015	1.4	EULER
6225.544	2.821 ± 0.002	3.583 ± 0.005	3.473 ± 0.004	3.895 ± 0.006	1.4	EULER
6232.501	2.831 ± 0.002	3.635 ± 0.005	3.400 ± 0.004	3.825 ± 0.005	0.8	EULER
6232.513	2.794 ± 0.010	3.588 ± 0.020	3.456 ± 0.008	3.869 ± 0.012	1.3	EULER
6236.552	2.816 ± 0.007	3.513 ± 0.012	3.392 ± 0.006	3.891 ± 0.008	5.7	EULER
6248.524	2.814 ± 0.008	3.511 ± 0.013	3.339 ± 0.006	3.837 ± 0.009	6.1	EULER
6251.522	2.773 ± 0.007	3.548 ± 0.013	3.348 ± 0.006	3.824 ± 0.009	5.2	EULER
6255.521	2.795 ± 0.005	3.552 ± 0.009	3.351 ± 0.006	3.811 ± 0.010	1.5	EULER
6387.892	2.479 ± 0.006	3.290 ± 0.011	3.221 ± 0.006	3.618 ± 0.007	7.7	EULER
6391.909	2.507 ± 0.007	3.293 ± 0.014	3.223 ± 0.007	3.622 ± 0.009	2.9	EULER
6396.909	2.470 ± 0.006	3.336 ± 0.012	3.229 ± 0.006	3.597 ± 0.008	6.5	EULER
6401.916	2.483 ± 0.007	3.317 ± 0.013	3.244 ± 0.007	3.619 ± 0.009	6.7	EULER
6405.897	2.481 ± 0.008	3.338 ± 0.016	3.201 ± 0.008	3.597 ± 0.011	1.5	EULER
6426.900	2.491 ± 0.010	3.308 ± 0.018	3.261 ± 0.009	3.582 ± 0.014	1.8	EULER
6435.872	2.502 ± 0.006	3.288 ± 0.010	3.276 ± 0.006	3.643 ± 0.008	6.9	EULER
6443.779	2.504 ± 0.013	3.299 ± 0.027	3.295 ± 0.013	3.580 ± 0.018	1.3	EULER
6447.755	2.507 ± 0.006	3.321 ± 0.012	3.284 ± 0.006	3.574 ± 0.007	4.3	EULER
6451.826	2.546 ± 0.006	3.282 ± 0.011	3.284 ± 0.006	3.618 ± 0.008	3.0	EULER
6455.899	2.563 ± 0.001	3.311 ± 0.003	3.253 ± 0.002	3.624 ± 0.003	1.9	EULER
6460.692	2.555 ± 0.009	3.353 ± 0.017	3.296 ± 0.008	3.595 ± 0.010	2.9	EULER
6468.728	2.553 ± 0.008	3.347 ± 0.016	3.317 ± 0.008	3.600 ± 0.010	2.6	EULER
6472.831	2.558 ± 0.007	3.313 ± 0.011	3.252 ± 0.006	3.645 ± 0.008	4.6	EULER
6476.840	2.565 ± 0.007	3.305 ± 0.013	3.274 ± 0.006	3.644 ± 0.008	3.7	EULER
6487.905	2.579 ± 0.006	3.289 ± 0.010	3.242 ± 0.005	3.571 ± 0.006	5.5	EULER
6491.597	2.555 ± 0.008	3.320 ± 0.016	3.288 ± 0.007	3.603 ± 0.009	2.3	EULER

Table 4—Continued

HJD	A1	A2	B	C	χ^2/N_{dof}	Source
6507.754	2.583 ± 0.006	3.325 ± 0.009	3.252 ± 0.005	3.629 ± 0.006	4.7	EULER
6515.817	2.596 ± 0.007	3.313 ± 0.012	3.277 ± 0.005	3.622 ± 0.007	3.1	EULER
6519.698	2.570 ± 0.005	3.276 ± 0.009	3.272 ± 0.005	3.705 ± 0.007	15.2	EULER
6523.581	2.565 ± 0.008	3.387 ± 0.015	3.310 ± 0.007	3.607 ± 0.009	3.7	EULER
6536.594	2.559 ± 0.008	3.355 ± 0.015	3.290 ± 0.007	3.651 ± 0.010	2.6	EULER
6541.644	2.579 ± 0.008	3.313 ± 0.013	3.240 ± 0.007	3.681 ± 0.010	4.5	EULER
6544.573	2.564 ± 0.008	3.345 ± 0.015	3.283 ± 0.007	3.674 ± 0.011	2.3	EULER
6548.724	2.604 ± 0.008	3.283 ± 0.013	3.203 ± 0.006	3.672 ± 0.008	6.0	EULER
6565.497	2.567 ± 0.009	3.349 ± 0.016	3.253 ± 0.007	3.597 ± 0.010	1.8	EULER
6565.509	2.546 ± 0.009	3.348 ± 0.018	3.237 ± 0.008	3.607 ± 0.011	1.6	EULER
6569.521	2.530 ± 0.005	3.353 ± 0.009	3.226 ± 0.005	3.647 ± 0.007	5.0	EULER
6572.558	2.548 ± 0.005	3.301 ± 0.008	3.203 ± 0.005	3.659 ± 0.006	8.6	EULER
6576.549	2.523 ± 0.006	3.315 ± 0.010	3.221 ± 0.005	3.666 ± 0.007	6.3	EULER
6581.604	2.541 ± 0.007	3.249 ± 0.013	3.203 ± 0.006	3.669 ± 0.009	6.1	EULER
6584.628	2.535 ± 0.008	3.281 ± 0.014	3.225 ± 0.007	3.615 ± 0.010	3.2	EULER
6599.552	2.515 ± 0.006	3.293 ± 0.010	3.209 ± 0.005	3.596 ± 0.006	5.5	EULER
6600.574	2.518 ± 0.005	3.249 ± 0.008	3.198 ± 0.005	3.596 ± 0.006	11.9	EULER
6604.538	2.527 ± 0.007	3.236 ± 0.013	3.191 ± 0.006	3.631 ± 0.008	3.9	EULER
6609.540	2.511 ± 0.005	3.262 ± 0.009	3.197 ± 0.005	3.590 ± 0.007	8.2	EULER
6612.521	2.519 ± 0.008	3.276 ± 0.015	3.190 ± 0.007	3.608 ± 0.009	3.1	EULER
6616.521	2.524 ± 0.009	3.328 ± 0.017	3.216 ± 0.007	3.560 ± 0.010	1.8	EULER
6745.906	2.533 ± 0.002	3.291 ± 0.003	3.310 ± 0.003	3.609 ± 0.004	2.9	EULER
6765.911	2.523 ± 0.006	3.388 ± 0.012	3.368 ± 0.007	3.555 ± 0.008	8.7	EULER
6775.899	2.492 ± 0.006	3.377 ± 0.010	3.371 ± 0.006	3.595 ± 0.007	7.1	EULER
6781.853	2.540 ± 0.007	3.307 ± 0.013	3.378 ± 0.006	3.602 ± 0.008	3.5	EULER
6789.900	2.543 ± 0.007	3.303 ± 0.013	3.363 ± 0.007	3.624 ± 0.009	2.4	EULER
6793.875	2.549 ± 0.007	3.327 ± 0.013	3.390 ± 0.008	3.636 ± 0.010	4.4	EULER
6797.924	2.551 ± 0.009	3.315 ± 0.018	3.309 ± 0.010	3.696 ± 0.014	2.4	EULER
6803.883	2.581 ± 0.007	3.346 ± 0.012	3.334 ± 0.006	3.659 ± 0.009	4.2	EULER
6805.832	2.574 ± 0.006	3.370 ± 0.011	3.364 ± 0.006	3.614 ± 0.007	5.3	EULER
6814.894	2.631 ± 0.006	3.331 ± 0.010	3.288 ± 0.005	3.655 ± 0.007	6.9	EULER
6818.896	2.631 ± 0.009	3.319 ± 0.015	3.278 ± 0.009	3.657 ± 0.012	2.6	EULER
6822.706	2.647 ± 0.013	3.363 ± 0.024	3.353 ± 0.011	3.604 ± 0.015	1.3	EULER
6834.749	2.596 ± 0.006	3.370 ± 0.010	3.370 ± 0.005	3.648 ± 0.007	6.8	EULER
6846.826	2.596 ± 0.006	3.331 ± 0.010	3.268 ± 0.005	3.677 ± 0.007	8.1	EULER
6874.560	2.578 ± 0.009	3.390 ± 0.017	3.279 ± 0.007	3.623 ± 0.010	1.7	EULER
6888.633	2.540 ± 0.006	3.350 ± 0.011	3.261 ± 0.006	3.671 ± 0.008	5.0	EULER
6908.528	2.539 ± 0.009	3.320 ± 0.018	3.292 ± 0.009	3.598 ± 0.012	1.8	EULER
6930.589	2.531 ± 0.006	3.301 ± 0.010	3.204 ± 0.005	3.646 ± 0.007	5.2	EULER
6937.568	2.531 ± 0.008	3.286 ± 0.015	3.194 ± 0.007	3.654 ± 0.011	3.1	EULER
6943.603	2.547 ± 0.005	3.267 ± 0.009	3.187 ± 0.005	3.614 ± 0.006	8.0	EULER
6947.525	2.525 ± 0.008	3.300 ± 0.014	3.203 ± 0.007	3.647 ± 0.010	3.1	EULER
6950.609	2.558 ± 0.008	3.274 ± 0.013	3.200 ± 0.006	3.601 ± 0.008	3.5	EULER
6954.612	2.542 ± 0.005	3.287 ± 0.009	3.208 ± 0.005	3.577 ± 0.006	11.6	EULER
6963.579	2.515 ± 0.008	3.284 ± 0.016	3.192 ± 0.007	3.610 ± 0.010	2.7	EULER
6974.526	2.505 ± 0.007	3.292 ± 0.014	3.224 ± 0.006	3.574 ± 0.008	3.1	EULER

Table 4—Continued

HJD	A1	A2	B	C	χ^2/N_{dof}	Source
6990.516	2.547 ± 0.013	3.272 ± 0.024	3.226 ± 0.011	3.549 ± 0.015	1.4	EULER
7113.905	2.549 ± 0.008	3.370 ± 0.016	3.300 ± 0.007	3.628 ± 0.009	2.3	EULER
7117.910	2.562 ± 0.011	3.362 ± 0.022	3.334 ± 0.010	3.587 ± 0.012	2.2	EULER
7123.909	2.568 ± 0.008	3.355 ± 0.016	3.313 ± 0.007	3.645 ± 0.010	2.4	EULER
7126.883	2.541 ± 0.006	3.376 ± 0.011	3.297 ± 0.006	3.639 ± 0.007	5.9	EULER
7138.858	2.544 ± 0.007	3.370 ± 0.013	3.273 ± 0.006	3.577 ± 0.008	3.2	EULER
7141.852	2.531 ± 0.007	3.364 ± 0.014	3.269 ± 0.006	3.588 ± 0.008	4.6	EULER
7145.844	2.560 ± 0.010	3.324 ± 0.019	3.238 ± 0.008	3.614 ± 0.011	1.6	EULER
7153.793	2.521 ± 0.008	3.354 ± 0.015	3.225 ± 0.007	3.603 ± 0.009	4.1	EULER
7157.888	2.535 ± 0.005	3.316 ± 0.008	3.193 ± 0.005	3.642 ± 0.007	7.8	EULER
7161.828	2.507 ± 0.007	3.391 ± 0.014	3.224 ± 0.007	3.595 ± 0.009	3.6	EULER
7170.829	2.490 ± 0.005	3.353 ± 0.009	3.209 ± 0.004	3.628 ± 0.006	4.3	EULER
7178.703	2.505 ± 0.014	3.247 ± 0.028	3.172 ± 0.011	3.578 ± 0.017	1.2	EULER
7186.875	2.450 ± 0.006	3.272 ± 0.011	3.132 ± 0.005	3.625 ± 0.008	4.2	EULER
7189.909	2.460 ± 0.007	3.233 ± 0.013	3.108 ± 0.006	3.620 ± 0.008	3.8	EULER
7193.878	2.428 ± 0.006	3.252 ± 0.010	3.091 ± 0.005	3.640 ± 0.007	10.5	EULER
7196.876	2.442 ± 0.007	3.226 ± 0.013	3.090 ± 0.006	3.652 ± 0.009	5.5	EULER
7200.681	2.441 ± 0.007	3.289 ± 0.013	3.130 ± 0.006	3.546 ± 0.008	3.3	EULER
7220.648	2.414 ± 0.007	3.248 ± 0.013	3.204 ± 0.006	3.547 ± 0.007	4.4	EULER
7227.605	2.390 ± 0.007	3.257 ± 0.014	3.205 ± 0.006	3.519 ± 0.008	2.7	EULER
7258.518	2.424 ± 0.007	3.286 ± 0.013	3.236 ± 0.006	3.457 ± 0.007	4.0	EULER
7263.564	2.412 ± 0.008	3.299 ± 0.016	3.274 ± 0.009	3.499 ± 0.011	2.7	EULER
7267.530	2.429 ± 0.005	3.296 ± 0.009	3.272 ± 0.005	3.492 ± 0.006	6.5	EULER
7270.537	2.440 ± 0.007	3.271 ± 0.014	3.291 ± 0.006	3.504 ± 0.008	2.5	EULER
7278.519	2.447 ± 0.006	3.315 ± 0.011	3.294 ± 0.006	3.501 ± 0.007	4.8	EULER
7293.582	2.441 ± 0.006	3.308 ± 0.010	3.242 ± 0.006	3.612 ± 0.007	9.5	EULER
7491.891	2.518 ± 0.007	3.307 ± 0.012	3.306 ± 0.006	3.615 ± 0.007	2.4	EULER
7507.870	2.508 ± 0.007	3.345 ± 0.014	3.328 ± 0.007	3.582 ± 0.008	2.2	EULER
7536.937	2.542 ± 0.020	3.304 ± 0.040	3.361 ± 0.020	3.643 ± 0.028	0.8	EULER
7557.851	2.575 ± 0.006	3.383 ± 0.011	3.335 ± 0.006	3.629 ± 0.008	4.1	EULER
7575.652	2.577 ± 0.006	3.353 ± 0.011	3.361 ± 0.005	3.575 ± 0.006	6.3	EULER
7590.677	2.570 ± 0.006	3.373 ± 0.011	3.371 ± 0.007	3.596 ± 0.009	5.4	EULER
7596.577	2.603 ± 0.010	3.332 ± 0.018	3.363 ± 0.008	3.593 ± 0.010	2.0	EULER
7599.776	2.579 ± 0.007	3.349 ± 0.013	3.315 ± 0.006	3.618 ± 0.008	4.5	EULER
7609.557	2.600 ± 0.007	3.350 ± 0.013	3.340 ± 0.006	3.607 ± 0.007	3.9	EULER
7647.656	2.590 ± 0.008	3.294 ± 0.015	3.322 ± 0.008	3.636 ± 0.010	3.0	EULER
7651.684	2.587 ± 0.006	3.314 ± 0.011	3.336 ± 0.006	3.618 ± 0.007	7.2	EULER
7671.581	2.581 ± 0.002	3.380 ± 0.004	3.373 ± 0.003	3.638 ± 0.004	3.3	EULER
7691.574	2.630 ± 0.007	3.336 ± 0.012	3.329 ± 0.006	3.640 ± 0.007	5.1	EULER
7696.536	2.618 ± 0.005	3.354 ± 0.008	3.337 ± 0.005	3.589 ± 0.006	21.9	EULER

Note. — HJD is the Heliocentric Julian Day –2450000 days. The goodness of fit of the image, χ^2/N_{dof}, is used to rescale the formal uncertainties by a factor of $(\chi^2/N_{dof})^{1/2}$. The Image A1-C columns give the magnitudes of the quasar images relative to the comparison stars.

REFERENCES

Bate, N. F., Floyd, D. J. E., Webster, R. L., & Wyithe, J. S. B. 2008, MNRAS, 391, 1955

Bate, N., Floyd, D.J.E., Webster, R.L., Wyithe, J.S.B., 2011, MNRAS, 731, 71

Blackburne, J. A., Pooley, D., Rappaport, S., & Schechter, P. L. 2011, ApJ, 729, 34

Bolton, A. S., Treu, T., Koopmans L. V. E., et al. 2008, ApJ, 684, 248

Bonvin, V. et al. 2017, MNRAS, 465, 4914

Bonvin, V. et al. 2018, A&A, in preparation

Chang, K. & Refsdal, S. Nature, 282, 561

Congdon, A. B., Keeton, C. R., & Osmer, S. J. 2007, MNRAS, 376, 263

Courbin, F, Eigenbrod, A., Vuissoz, C. & Magain, P. 2005 in IAU Symp. 225, Gravitational Lensing Impact on Cosmology, ed. Y. Mellier & G. Meylan (Cambridge: Cambridge University Press), 297

DePoy, D.L., Atwood, B., Belville, S.R., Brewer, D.F., Byard, P.L., Gould, A., Mason, J.A., O'Brien, T.P., Pappalardo, D.P., Pogge, R.W., Steinbrecher, D.P., & Tiega, E.J., 2003, SPIE, 4841, 827

Edelson, R., Gelbord, J., Cackett, E., et al. 2017, ApJ, 840, 41

Eigenbrod, A., Courbin, F., Meylan, G., Vuissoz, C. & Magain, P. 2006, A&A, 451, 759

Fasnaugh, M.M. wt al. 2018, ApJ, 854, 107

Fohlmeister, J., Kochanek, C.S., Falco, E.E., Wambsganss, J., Oguri, M. & Dai, X., 2013, ApJ, 764, 186

Giannini, E. et al. 2017 A&A, 597, 849

Gould, A. 2000, ApJ, 535, 928

Hainline, L. J., Morgan, C. W., Beach, J. N., et al. 2012, ApJ, 744, 104

Hainline, L. J., Morgan, C. W., MacLeod, C.L., et al. 2013, ApJ, 774, 69

Hinshaw, G., et al. 2009, ApJS, 180, 225

Keeton, C. R. 2001, arXiv:astro-ph/0102340

Kochanek, C.S., 2002, ApJ, 578, 25

Kochanek, C. S. 2004, ApJ, 605, 58

Kochanek, C. S., Morgan, N. D., Falco, E. E., et al. 2006, ApJ, 640, 47

Lehár, J., Falco, E. E., Kochanek, C. S., et al. 2000, ApJ, 536, 584

MacLeod, C. L., Morgan, C. W., Mosquera, A., Kochanek, C. S., Tewes, M., Courbin, F., Meylan, G., Chen, B., Dai, X., Chartas, G. 2015, ApJ, 806, 258

Mediavilla, E., Muñoz, J. A., Kochanek, C. S., et al. 2011, ApJ, 730, 16

McHardy, I. M., Connolly, S. D., Peterson, B. M., et al. 2016, AN, 337, 500

Morgan, N.D., & Caldwell, J.A.R., & Schechter, P.L., & Dressler, A., & Egami, E., & Rix, H.-W. 2004, AJ, 127, 2617

Morgan, C.W., Kochanek, C.S. Morgan, N.D. & Falco, E.E. 2006, ApJ, 647, 874

Morgan, C. W., Kochanek, C. S., Dai, X., Morgan, N. D., & Falco, E. E. 2008b, ApJ, 689, 755

Morgan, C. W., Kochanek, C. S., Morgan, N. D., & Falco, E. E. 2010, ApJ, 712, 1129

Morgan, C. W., Hainline, L. J., Chen, B., et al. 2012, ApJ, 756, 52

Mortonson, M.J., Schechter, P.L. & Wambsganss, J. 2005, ApJ, 628, 594

Mosquera, A. M., & Kochanek, C. S. 2011, ApJ, 738, 96

Motta, V., Mediavilla, E., Rojas, K., et al. 2017, ApJ, 835, 132

Navarro, J. F., Frenk, C. S., & White, S. D. M. 1996, ApJ, 462, 563

Poindexter, S. Morgan, N.D., Kochanek, C.S. & Falco, E.E. 2007, ApJ, 660, 146

Pooley, D., Blackburne, J. A., Rappaport, S., & Schechter, P. L. 2007, ApJ, 661, 19

Pooley, D, Rappaport, S., Blackburne, J.A., Schechter, P & Wambsganss, J. 2012, ApJ, 744, 111

Refsdal, S. 1964, MNRAS, 128,307

Schechter, P. L., & Wambsganss, J. 2002, ApJ, 580, 685

Schechter, P. L., Pooley, D. Blackburne, J.A & Wambsganss, J. 2014, ApJ, 793, 96

Shakura, N. I., & Sunyaev, R. A. 1973, A&A, 24, 337

Sluse, D., Chantry, V., Magain, P., Courbin, F. & Meylan, G. 2012, A&A, 538, 99

Suyu, S. H., Bonvin, V., Courbin, F., et al. 2017, MNRAS, 468, 2590

Tie, S.S. & Kochanek, C.S. 2018, MNRAS, 473, 80

Treu, T., & Koopmans, L. V. E. 2004, ApJ, 611, 739

Vuissoz, C. et al. 2008, A&A, 488, 481

Wambsganss, J., Schmidt, R. W., Colley, W., Kundić, T., & Turner, E. L. 2000, A&A, 362, L37

Wyithe, J. S. B., Webster, R. L., & Turner, E. L. 2000, MNRAS, 312, 843